Design and Testing of a Blended Wing Body with Boundary Layer Ingestion Nacelles at High Reynolds Numbers (Invited)

Richard L. Campbell*, Melissa B. Carter† and Odis C. Pendergraft, Jr. ‡
NASA Langley Research Center, Hampton, VA 23681

Douglas M. Friedman§ and Leonel Serrano¶
Boeing Phantom Works, Huntington Beach, CA 92647

A knowledge-based aerodynamic design method coupled with an unstructured grid Navier-Stokes flow solver was used to improve the propulsion/airframe integration for a Blended Wing Body with boundary-layer ingestion nacelles. A new zonal design capability was used that significantly reduced the time required to achieve a successful design for each nacelle and the elevon between them. A wind tunnel model was built with interchangeable parts reflecting the baseline and redesigned configurations and tested in the National Transonic Facility (NTF). Most of the testing was done at the cruise design conditions (Mach number = 0.85, Reynolds number = 75 million). In general, the predicted improvements in forces and moments as well as the changes in wing pressures between the baseline and redesign were confirmed by the wind tunnel results. The effectiveness of elevons between the nacelles was also predicted surprisingly well considering the crudeness in the modeling of the control surfaces in the flow code. A novel flow visualization technique involving pressure sensitive paint in the cryogenic nitrogen environment used in high-Reynolds number testing in the NTF was also investigated.

Nomenclature

c	=	local wing chord
C_D	=	drag coefficient
C_f	=	stream-wise component of skin-friction coefficient
C_L	=	lift coefficient
C_m	=	moment coefficient
C_P	=	pressure coefficient
l	=	length of design station
L/D	=	lift-to-drag ratio
M_∞	=	free-stream Mach number
Re_c	=	Reynolds number based on mean aerodynamic chord
x	=	distance in stream-wise direction
z	=	distance in vertical direction
α	=	angle of attack, degrees
η	=	wing semi-span station

* Senior Research Engineer, Configuration Aerodynamics Branch, M/S 499, AIAA Associate Fellow.
† Aerospace Engineer, Configuration Aerodynamics Branch, M/S 499, AIAA Member.
‡ Aerospace Engineer, Configuration Aerodynamics Branch, M/S 499, AIAA Senior Member.
§ Boeing Associate Technical Fellow, Flight Sciences, M/S H013-A319, AIAA Associate Fellow.
¶ Aerospace Engineer, Flight Sciences, M/S H013-C328.

I. Introduction

In the last decade, there has been a growing interest in the Blended Wing Body (BWB) concept as a way of addressing the rising cost of fuel, the increasing number of air travelers, and environmental concerns such as emissions and noise. Recognizing the potential of this type of aircraft, NASA sponsored a study in 1994 to investigate the technical and commercial feasibility of the concept. The study team consisted of several NASA centers and universities, with McDonnell Douglas serving as the program coordinator. In the 2002 AIAA Wright Brothers Lecture[1], Liebeck gives an excellent review of the results of that study along with a summary of work completed after McDonnell Douglas merged with Boeing. This and other studies[2-4] have indicated fuel savings on the order of 30% for the BWB in comparison with other large aircraft (B747, A380), along with significant reductions in size and weight for a given mission. The large usable internal volume makes the BWB an attractive candidate as a freighter or tanker, with the potential of refueling multiple aircraft simultaneously. The simplicity of the configuration suggests a reduction in part count with a corresponding reduction in manufacturing costs. Additional savings could result from a unique approach to commonality if a family of BWB aircraft was developed. In addition to the reduced emissions associated with a lower fuel-burn rate, another environmental benefit would be a reduction in noise levels. Most of the configurations studied have engines mounted near the trailing edge on the upper surface of the wing, which tends to shield the inlet noise[5] and avoids the issue of exhaust noise reflecting off the lower surface of the wing, as with current large transports. If fuel prices allow increased speed to become a practical marketing advantage, the BWB has a natural area ruling[6] that, perhaps combined with other technologies such as the slotted-wing[7], could allow a cruise speed in the Mach 0.93-95 range to be economically obtained.

While these studies indicated some significant benefits for the BWB relative to the conventional "tube and wing" configurations, they also pointed out a number of challenges that would have to be solved before the aircraft would be technically and economically viable. The elimination of the tail makes requirements such as trim (at cruise and take-off/landing), low deck angle, and engine-out control more difficult to address. The non-circular fuselage cross-section presents a challenge for handling the pressurized cabin loads and has spawned several new structural approaches that will most likely require composite materials. Other concerns for a passenger version of a BWB include ride quality, lack of windows, and emergency egress. As Liebeck points out, significant progress has been made on many of the above concerns and research on technologies applicable to a BWB continues within the NASA Vehicle Systems Program.

As noted above, most versions of the BWB have the engines mounted above the upper surface of the wing near the trailing edge (see Fig. 1). Initial configurations proposed mounting the engines on the wing surface with a "mail slot" inlet to ingest the boundary layer. While some early, unpublished system studies indicated very large performance benefits due to the reduction in ram drag, problems with inlet conditions were deemed intractable. At this point, Boeing decided to focus their development efforts using nacelles mounted on struts to avoid problems of surface integration and the inlet flow distortion that comes from ingesting the boundary layer. However, later systems studies indicated that less extreme boundary layer ingestion (BLI) inlet configurations could still lead to a number of benefits, including reduced ram drag, lower structural weight, and less wetted area than a strut-mounted engine configuration. In addition, having the thrust vector closer to center of gravity would produce less nose-down pitching moment, reducing trim problems along with control surface size and power requirements. Reference 8 indicates that about a 10% reduction in fuel burn could be achieved if the propulsion/airframe integration (PAI) for the BLI nacelles can be improved and the flow distortion can be reduced to acceptable levels.

Several research efforts have shown some success in addressing the PAI and distortion problems. Rodriquez[9,10] applied computational fluid dynamic (CFD)-based optimization to a 3-engine BWB/BLI configuration and was able to reduce drag and improve inlet pressure recovery while holding distortion at a fixed level. Apparently some effort was also made to reduce distortion levels, but it was concluded to be "nearly impossible", at least for the inlet/duct geometry and the design variables used. Research has also been underway within the NASA Ultra-Efficient Engine Technology (UEET) Project to address both the flow distortion and PAI problems. In Ref. 11, active flow control was applied to a generic BLI inlet/S-duct configuration to reduce flow distortion. The results of their CFD and experimental studies indicate that significant improvements in inlet distortion levels can be obtained using pulsed-jet flow control. Also under UEET, an effort was initiated to extend and apply advanced CFD-based design methods to the BLI PAI problem and to verify the results through high-Reynolds number tests in the National Transonic Facility (NTF). The approach and results from both the CFD design and the wind tunnel tests are described in the following sections of this paper.

II. CFD Design and Analysis

A. Design Method Selection

The PAI design effort in the UEET project was initiated because of some encouraging results obtained at the end of the NASA Advanced Subsonic Technology (AST) Program. In an unpublished study, the CDISC design method[12] coupled with the OVERFLOW overset grid Navier-Stokes flow solver[13] (OVERDISC) was applied to an early twin-engine version of the BWB. The design modified the wing surface as well as the outer nacelle surface, although grid movement difficulties made it necessary to keep the nacelle-wing intersection fixed. In spite of this restriction, OVERDISC was able to nearly eliminate the PAI-related shocks and improve the lift/drag ratio by 6.5%.

Although the results indicated that the design method was efficient and effective, the initial grid generation and subsequent grid movement during the design proved to be somewhat cumbersome. It was therefore decided to try using design methods based on unstructured grid flow solvers for further design work on newer configurations. Two unstructured grid Navier-Stokes flow solvers, each coupled with a different design approach, were selected. The first was the USM3D flow solver[14], part of the TetrUSS software system[15], coupled with the CDISC design method. The second was the FUN3D flow solver that uses adjoint-based optimization for design[16]. A third option was to continue using OVERDISC and improve the grid movement method if the unstructured methods did not prove to be adequate.

Since the unstructured grid flow solvers were not as well validated at that time as structured grid methods, a preliminary study was undertaken to evaluate their accuracy in predicting the flow characteristics for a clean-wing (no nacelles) version of the BWB that had been tested in the NTF as part of the AST Program. A picture of the model in the wind tunnel is shown in Fig. 2. Note that since there is not a typical fuselage, a large fairing was needed on top of the wing to cover the sting. The OVERDISC method was used to modify the fairing outer mold line to minimize the disturbance to the original wing pressures.

Each of the flow solvers (USM3D, FUN3D, and OVERFLOW) was run at a series of angles of attack at the cruise Mach number of 0.85 and a Reynolds number of 25 million for comparison with the wind tunnel data. A comparison of the USM3D results with experimental wing pressures at an inboard wing station near where a nacelle would be located is given in Fig. 3. In general, the computations matched the experimental data very well, and this level of correlation was typical of that seen at all span locations. The computed results indicate a slight acceleration ahead of the shock, but since there is no experimental data at that location, it is unclear how accurately the shock position and strength were matched, though there is good correlation downstream. Overall force and moment comparisons are shown in Fig. 4, where it can be seen that the USM3D results correlated very well with the experimental data. The levels are matched in and above the cruise range (C_L = 0.4-0.5) and even the pitch break is predicted fairly accurately.

The initial comparisons with experimental force and moment data for both FUN3D and OVERFLOW indicated that the correlation was worse than that seen with USM3D. Since there were also some difficulties with using the FUN3D adjoint solver on large grids at that time and the program schedule was tight, it was decided to proceed with USM3D/CDISC in the design phase. Subsequent investigations found that geometry and grid discrepancies led to the poor correlation with data for the other two codes. The problem with running large grids in the FUN3D adjoint solver has also been resolved.

B. Design Method Description

One additional reason for selecting the USM3D/CDISC design system for the PAI design effort was the availability of a zonal design capability that had recently been implemented. This option allows a user to do local redesign using a subset of the full grid, which can significantly reduce the time required to develop a successful design strategy. This design system consisted of the PREDISC graphical pre/post-processor, codes for extracting and re-inserting the zonal design regions, the USM3D flow solver, the CDISC design module, and several auxiliary codes to link the flow solver and design module. The design process and its various components are described below.

1. USM3D Flow Solver

The zonal design process begins by running USM3D to obtain a flow solution for the full-grid baseline configuration at the design conditions. The USM3D code is a cell-centered, finite-volume Navier-Stokes flow solver

that uses Roe flux-difference splitting[17] to compute inviscid flux quantities across the faces of the tetrahedral cells. Several options for turbulent closure are available: the one-equation Spalart-Allmaras (S-A) model[18] (with and without a wall function), and several two-equation models, including Menter's Shear Stress Transport (SST) model[19]. Work is currently underway to add a multi-grid capability to the code[20], but it was not available at the time of this study. Past experience has shown that multi-grid is very beneficial for design in that the influence of changes can be quickly spread through the flow-field. The parallel version of the flow solver was run in the implicit mode for this study. The wall function option with the S-A turbulence model was used to reduce the number of grid points required to model the boundary layer, and the minmod limiter was turned on to help stabilize the code during the design process (subsequent work indicates that this probably was not needed). The code was modified to include a new boundary condition type for use on the zonal grid box faces. Setting this boundary condition type freezes current flow conditions on the zonal faces and at the corresponding ghost cell centers.

2. Zonal Grid Extraction

The grid and resulting solution files from USM3D are read into PREDISC where the user graphically defines the zonal region of interest. The shape of the region is currently limited to a rectangular box, but other simple 3-D shapes such as a cylinder would be easy to include. Once the box is defined, the extraction code identifies all cells that are completely within the box and marks the new zonal faces. The code then renumbers the new points, cells, and faces and writes out all files needed to run the zonal case (grid, restart, connectivity, etc.). A point/cell/face-mapping file is also saved to allow the modified zonal grid and/or restart files to be reinserted into the original full grid files after design. The zonal grid case is often an order of magnitude or more smaller than the full grid case and can easily be run on a single-processor workstation or PC.

3. CDISC Design Method

After the zonal grid is extracted, PREDISC is used to select the components and surfaces for design and to define the location and type of design station. A design station can be defined along surface patch boundaries or at the intersection of a plane with the design surface, and the stations may be distributed across a component as a series of parallel (wing, winglet) or radial (fuselage, nacelle) planes. PREDISC will extract and display the current surface geometry and pressure distribution at each design station. In addition, the user can try different combinations of flow and geometry constraints, automatically run CDISC, and plot the resulting target pressures and design geometries to help evaluate different constraint strategies. The PREDISC code will then write out all files needed by a similar geometry/pressure extraction module for the actual design run.

The CDISC module is a knowledge-based design method that has been coupled with a variety of 2-D and 3-D flow solvers ranging from potential flow to Navier-Stokes and, for the latter category, has been used with structured, overset, and unstructured grids. The code uses specified flow/geometry relationships developed from analytical or empirical studies to compute geometry changes based on the difference between current and target flow quantities. This eliminates the need to compute sensitivity derivatives and allows the design to converge in parallel with the flow solution, thus greatly reducing the time required for a design. The design time is further reduced by the use of flow constraints to automatically develop the target distribution from the current values of flow quantities such as pressure or skin-friction coefficients. These constraints address common engineering design variables such as span load, section lift and pitching moment coefficients, and shock strength. This approach has generally been more robust than manually specifying a fixed input target pressure in that it tends to avoid problems such as an incorrectly specified attachment line location or pressure level. In addition to the flow constraints, geometry constraints such as thickness, curvature, volume and leading edge radius are available to address requirements from other disciplines such as structures and manufacturing.

4. Grid Modification

After the geometry changes at the design stations are determined with CDISC, two codes are used to modify the CFD grid for further analysis in the flow solver. The first code does a linear lofting of the changes at the design stations on to the previous surface grid, with special provisions for absorbing changes on a component with a single design station (e.g., adjust the fuselage grid for changes to the wing/fuselage intersection). The second code adjusts the volume grid to accommodate these changes. It has been found that this process is more robust if the changes are made with respect to the original grid and design surface geometries.

For volume grid adjustment, the grid points are assigned to layers, with the first layer being points on a solid geometry surface, the second layer consisting of points connected to layer one points, and so forth until all points are labeled. The movement of each point is determined by the displacement of the nearest point in the previous layer,

with a decay function applied to points outside the boundary layer region. This initial movement can create cells with negative volumes and/or large volume differences between cells with a common face. The code will adjust these cells in an attempt to eliminate all negative volume cells. Options to renormalize the grid in the boundary layer region and to adjust cells with a common face so that the ratio of their volumes is less than a specified value were also used in the current study. After the grid is successfully modified, it is returned to the flow solver for further analysis by restarting from the previous solution.

The design process described in the sections above is typically repeated for 10-20 cycles and the results evaluated using PREDISC. If the results are stable, converged, and indicate the desired flow improvements with a reasonable surface geometry, the new zonal grid can be reinserted in the full grid for further analysis to confirm the global impact of the design. If needed, additional design can be carried out on the full configuration using the design strategy developed using the zonal approach.

C. PAI Design Approach

For the PAI design, a 3-engine, 450-passenger version of the BWB was chosen as a baseline. A semi-span unstructured grid consisting of about 4 million tetrahedral cells was generated using VGRID[21], part of the TetrUSS software system. The surface grid, mirrored to illustrate the full configuration, is shown in Fig. 5, with a close-up view of the nacelle area on the right-hand side of the figure. The original grid (shown) was generated using a powered-nacelle geometry provided by Boeing. Since the wind tunnel validation tests would be done with flow-through nacelles, the grid was modified using PREDISC and other codes to increase the nacelle exit area so that the desired cruise mass flow ratio of about 0.72 was recovered.

Results from the initial USM3D flow analysis (Fig. 6) reveal several areas where the flow characteristics could be improved. In Fig. 6a, a weak-to-moderate shock can be seen near the lip of each nacelle. For the outboard nacelle, the shock is stronger on the inboard side, suggesting that a re-alignment of that nacelle along with some re-contouring of the nacelle/wing fairings should provide a reduction in wave drag. Fig. 6b shows a plot of contours of a function indicating the condition of the boundary layer in the region of the nacelles (referred to as the SEP or separation function). This function is based on levels of the stream-wise component of the skin-friction coefficient and indicates areas of weak boundary layer (green), insipient separation (yellow), and separation with reverse flow (red). As can be seen, significant areas of separation are present ahead of each inlet, with weakened boundary layer flow spilling around and contaminating the flow over the elevon between the nacelles. Reducing the separation on the elevon should provide a profile drag benefit and may improve the effectiveness of this control surface.

It was therefore decided to first use PREDISC to manually adjust the outboard nacelle cant angle and smooth the fairings around the base of each nacelle before proceeding to a CDISC-based design. A tow-out angle of 3 degrees was found to give similar, very weak shocks on each side of the outboard nacelle and, along with the smoothing, reduced the maximum local Mach number on the nacelles to less than 1.08. In addition to reducing the wave drag, the weakening of the shocks had a favorable effect on the boundary layer on the wing between the nacelles.

Using this new geometry as a starting point, a 3-zone CDISC design was initiated. As shown in Fig. 7, zonal boxes were defined around each of the nacelles and the elevon using sizing criteria from Ref. 22. Because the design runs are made using only the grid cells contained in each zonal box, design times were reduced by factors of 5, 3 and 20 for the inboard, outboard and elevon zones, respectively, compared with designing using the full grid. This proved to be extremely useful in that a number of design runs were required to refine the design strategy for each of the components. The general design approach was to attempt to reduce the size of the separated flow regions in front of each of the inlets, then plug these results back into the full grid and update the flow solution so that any improvements in the flow spilling around the nacelles would be reflected in the flow over the elevon. The central zonal grid would then be extracted for design of the elevon surface itself to clean up any remaining flow problems.

There are several approaches available in CDISC for addressing separated flow, depending on the source of the adverse pressure gradient that causes it. For cases where the pressure field from a leading-edge attachment line slows the flow on an intersecting surface (e.g., wing/fuselage intersection), there are options in CDISC to grow a planform fillet or "horn" on the wing leading edge. If the separation is due to a strong shock on an airfoil section, a combination of flow constraints can be used to reduce the shock Mach number while maintaining lift. Constraints have also been developed to adjust pitching moment via aft loading to limit airfoil trailing edge separation. Finally, if the separation is due to an adverse pressure gradient caused by a local surface bump or component interaction away from a leading or trailing edge, constraints that limit and smooth local surface pressures and/or curvatures have proven effective.

In all of the approaches above, the skin friction characteristics on a surface are indirectly addressed through the application of pressure-based constraints. There is also a capability in CDISC based on the work of Green[23] that modifies a surface directly based on the difference between the current skin-friction distribution and a target

distribution. Though more direct than the pressure-based constraints, this approach has been found to be much slower since more flow iterations were required per design cycle to adequately reflect the skin friction change rather than a pressure change resulting from a given geometry modification. In view of this, pressure-based constraints were selected for this study, with the specific approach illustrated in the next section.

D. CDISC Design Results

The CDISC design was initiated using the zonal grid containing the inboard nacelle. Although some of the flow separation in front of the inlet is related to the lip attachment line pressures, there is also a significant influence of the reduced flow velocities in the duct itself. Therefore, apart from some minor filleting that occurred as a result of smoothing the nacelle/wing fairing, it was decided to try to reduce the flow separation by limiting the pressure levels on the wing surface approaching the inlet. A series of stream-wise design stations were defined that extended from the inlet to the rear wing spar approximately 2 nacelle diameters ahead of the inlet. Several of the design stations actually extended into the inlet in an effort to reduce the region of separated flow there. As can be seen in Fig. 8, the regions of weak boundary layer and flow separation ahead of the nacelles correlated fairly well with levels of pressure coefficient greater than 0.2. Note that the baseline SEP function levels shown in Fig. 6b are different from those in Fig. 8a because the latter results include the effects of the minmod limiter in USM3D, which had been invoked to improve convergence during the design. Based on the C_P-SEP correlation, the target pressure constraint strategy illustrated in Fig. 9a was implemented. First, the stream-wise location where the pressure coefficient is first greater than 0.2 is determined and a pressure level constraint is implemented to keep the C_P less than 0.2 for a distance of x/l=0.1 aft of that point. A small region of neutral pressure gradient such as this has been found to be beneficial in controlling the boundary layer growth before the trailing-edge pressure recovery on supercritical airfoils. Next, the target pressures are defined to be linear between this point and the current trailing edge value, then the target distribution is smoothed aft of x/l=0.5. In keeping with the recommendations of Ref. 22, the active design region began at x/l=0.2 and geometry smoothing was applied to control any kinks that may tend to form at the beginning of a partial-chord design region. Each successive design cycle develops a new target pressure distribution by applying the same constraint strategy to the current analysis pressures, except that the original location of the first occurrence of C_P=0.2 is always used.

The results for a design station about midway between the centerline and side of the nacelle are shown in Fig. 9b and 10. As can be seen, the final design pressure coefficients match the target distribution fairly well and maintain lower values relative to the baseline over the aft end of the design region. There was concern that, though the milder pressure gradient in the region between x/l=0.4 and 0.7 should improve the skin friction levels there, the steeper adverse pressure gradient aft of that region might actually make the separation going into the inlet worse. This was not the case, as illustrated in Fig. 10a; instead, there was a significant increase in the skin friction level from x/l=0.3 aft. As also shown in Fig. 11, the regions of reverse flow and most of the insipient separation has been eliminated and there is some improvement in the boundary layer health over the inboard side of the elevon. Figure 10b shows that a bump was created above the original surface to produce these changes. It should be noted that this bump does not function as a diverter, but simply improves the flow characteristics of the boundary layer that is ingested.

The same general design strategy was used for the outboard nacelle zone, with the results shown in Fig. 12. Although the boundary layer characteristics were improved, the change was not as dramatic as for the inboard nacelle. This is probably due to the shorter design region available since the rear wing spar is about a nacelle diameter closer to this inlet than to the inboard inlet. Nevertheless, the modifications ahead of the nacelle, combined with the effects of reducing the nacelle shock by towing the nacelle out, nearly eliminated the insipient separation region on the outboard portion of the elevon.

A similar design strategy was employed on the elevon itself, except a C_P constraint level of 0.15 was used instead of 0.2, based on C_P-SEP correlations for this area. As can be seen in Fig. 13, the regions of weakened boundary layer and insipient separation have been significantly reduced. The stream-wise pressure and skin-friction changes were similar to those shown in Fig. 9b and 10a. It is believed that the shape of the new skin-friction distribution should delay the forward progression of separation as angle of attack or elevon deflection is increased.

As a check on the zonal design method, the new grids from all three zones were inserted back into the full grid and the flow solver was run starting from the baseline solution. The results from this analysis are shown in Fig. 14 and can be seen to be nearly identical to the individual zone results in Figs. 11b, 12b and 13b. The flow on the elevon is slightly different, possibly due to circulation effects since the changes in that zonal design did not necessarily conserve lift. A full-grid analysis with the minmod limiter turned off for more accurate prediction of drag was also run, with the results indicating that the design had about a 1.3 per cent improvement in lift-to-drag ratio relative to the baseline. The pitching moment was also slightly less negative, which should provide a trim drag benefit.

E. CFD Elevon Evaluation

In addition to reducing the drag at cruise, one of the goals in improving the boundary layer characteristics on the elevon was to make the control surface more effective when deflected. Developing a new unstructured grid with elevon edges and gaps represented would have been the most accurate way to assess any improvement in elevon effectiveness for the new design, but a detailed geometry model for the design had not been developed from the final grid at that time. Since CDISC has a simple flap constraint option, it was decided to evaluate it even though the grid movement scheme would provide only a crude modeling of the elevon edges with no gaps. A shaded representation of the CFD model of the new design with the elevon deflected 5 degrees trailing-edge down is shown in Fig. 15. The boundary-layer-tailoring bumps developed in the design can also be seen ahead of the inlets.

Figure 16 compares the boundary layer characteristics for the new design for elevon deflections of 0 and 5 degrees. The increase in deflection angle enlarged the area of weakened boundary layer and there was some forward progression of the insipient separation and reverse flow regions near the elevon edges. (It should be noted that the contours for the un-deflected case are from the analysis with the minmod limiter turned off and thus appear different from those shown for the baseline in previous design-related figures). As can be seen in Fig. 17, the baseline configuration with a 5-degree elevon deflection has significantly more separated flow than the new design, with the weakened boundary layer region covering nearly the entire control surface. At these conditions, the new design had about a 1.5 percent improvement in L/D relative to the baseline; however, the change in pitching moment for the 5-degree deflection was approximately the same for the baseline and redesign, indicating no increase in effectiveness.

F. Evaluation of Model Mounting System

The previous test of a wing-only BWB model in the NTF used a rear-mounted straight sting with a sting fairing as shown on Fig. 1. This approach would obviously not work for this case where the key region of interest is in the vicinity of the aft-mounted nacelles. Several other model support approaches were considered, including a yoke attached to the wing tips, a lower plate, and a lower swept strut or blade. A lower swept strut mounted toward the back of the model was considered for the previous NTF test, but CFD analysis indicated that the interference would significantly increase the strength of shocks on both the upper and lower surfaces. An examination of the lower surface pressures for the current configuration, however, revealed that lower surface velocities were fairly low over the front half of the model centerline; thus, the superimposed velocities of the strut would be less likely to create strong shocks if the strut were mounted farther forward.

This concept was evaluated using CFD for a wing-only (no nacelles) configuration and a sting geometry derived from an upper-strut mount that simulates the vertical tail on a conventional jet transport. The computations were performed using OVERFLOW with the S-A turbulence model. The wing-only grid had 6 zones with over 6 million grid points, whereas the wing-strut cases had about twice as many zones and almost three times as many grid points. These initial computations indicated fairly low levels of interference, so a detailed definition of the actual strut geometry was developed and analyzed. The strut geometry along with the computed pressure contours at the cruise condition is shown in Fig. 18. A very weak shock is visible on the wing lower surface and the blade portion of the sting, but in general the interference appears to be very benign. Figure 19 shows the upper and lower surface pressure contours for the model with and without the sting, with Fig. 20 showing chord-wise pressure distributions at 3 span stations. As can be seen, the effects of the strut are fairly local, with almost no impact on the upper surface pressures. A number of runs at different angles of attack and Mach numbers were then made with the two configurations to develop corrections for sting effects to be applied to the wind tunnel data.

The predicted strut corrections for the lift, drag, and pitching-moment coefficients as a function of angle of attack have been plotted in Fig. 21. The increments have been converted to a percentage of the cruise value of the respective parameter obtained from the wind tunnel data for the baseline BLI configuration. Also included on each plot is the linear approximation that was used to correct the wind tunnel data. As can be seen in Fig. 21a, the lift correction is nearly constant and less than 1 percent of the cruise lift coefficient. The drag correction varies more with angle of attack, but is still fairly linear. The magnitude of the correction at the cruise angle of attack of about 4 degrees (about 3 percent) is similar to that of the rear-mounted sting used in the original AST BWB test. The pitching moment correction is a much larger percentage of the cruise value, in part because the cruise value is small since the configuration is close to being trimmed. The corrections are also less linear than for lift or drag. For performance comparisons between the baseline and redesigned BLI configurations at cruise, the linear estimate used for data reduction is probably adequate; for accurate stability evaluations, however, a non-linear model and a broader angle of attack range of CFD results would be required.

III. Wind Tunnel Test

A. Facility

An experimental evaluation of the BWB configurations was conducted in the National Transonic Facility (NTF) at the NASA Langley Research Center. The NTF is a pressurized, fan-driven, closed-circuit, continuous-flow wind-tunnel. The test section's cross-section is 8.2 by 8.2ft, and has a length of 25ft. The floor and ceiling of the test section are slotted (6 percent open), while the sidewalls are solid. The facility is able to operate in warm temperatures using dry air, or at warm to cryogenic conditions using nitrogen gas. The NTF can test at temperatures ranging from 150°F to –320°F, Mach numbers ranging from 0.2 to 1.2, absolute pressures ranging from 15 to 130 psi, and a maximum Reynolds number of 146×10^6 per foot at Mach 1.0.[24]

B. Model

The BWB model, a 2-percent scaled version of the 450-1L configuration, was designed to accommodate the testing goals of several research groups. In addition to the performance testing conducted under the UEET project, a stability and control test under the EASI Project in the Vehicle Systems Program is scheduled for 2005. In order to meet the goals of both programs, the model was made with many interchangeable parts. There are 4 primary configurations: a clean wing (no nacelles), pylon-mounted nacelles, and the baseline and redesigned BLI nacelles (Fig. 22–25 respectively). The model has a total of 12 elevons that can be individually deflected. In addition, the wings can terminate in either a revolved wing tip (Fig. 22) or a winglet (Fig. 26).

Since the goal of this wind tunnel test was to verify the predicted performance improvements for the new design relative to the baseline, the model was designed to interface with a blade sting (Fig. 27) to minimize any impact on the flow in the nacelle region. The blade connects to the balance that is attached to the model via a strut block that can be changed to allow testing at various yaw angles. During the performance testing in the current study, the yaw angle was held constant at zero degrees.

The model and sting were made out of a maraging steel and the model surface finish was 2–4 micro-inches. The model, including all the interchangeable parts, had over 400 pressure ports. Due to limited space within the model (Fig. 28), only 4 electronically-scanned pressure (ESP) modules could be used. Consequently, only 248 pressure ports could be monitored at a time.

C. Test Conditions

The primary objective of the test was to evaluate the performance of the redesigned BLI nacelle configuration relative to the baseline geometry at realistic operating conditions (high Reynolds numbers, cruise Mach and angle of attack ranges). Given the size of the model, the maximum Reynolds number obtainable was 75 million (this is roughly equivalent to the 25 million Reynolds number of the previous wing-only AST test when adjusted to the same reference chord). The cruise Reynolds number for the full-scale aircraft is approximately 180 million.

All four configurations, with revolved wing tips and elevons at zero degrees, were tested at cryogenic conditions (–250°F), at Mach numbers ranging from 0.84 to 0.86, and angles of attack ranging from –1 to 8 degrees. The two BLI configurations were also tested with the two innermost elevons deflected 5 degrees (Fig. 29). Additionally, the clean wing configuration was tested at Mach numbers ranging from 0.5 to 0.88.

The clean wing and pylon-mounted nacelle configuration with winglets were also tested in warm air (120°F). The clean wing was tested at Reynolds numbers of 10 and 16 million, Mach numbers ranging from 0.5 to 0.88, and angles of attack of –3 to 11 degrees. The pylon-mounted nacelles with winglets was tested at Reynolds numbers of 2.4, 3.7, and 10 million, Mach numbers ranging from 0.2 to 0.9, and angles of attack from –3 to 16 degrees.

D. Repeatability

The test included two repeatability runs at the cruise Mach number of 0.85 for each of the configurations. Figures 30, 31, and 32 show the repeatability results of C_L, C_D, and C_m, respectively, for the baseline BLI nacelles. These figures, which are representative of all configurations, show that repeatability of the data was generally quite good, although the agreement for drag between runs deteriorates slightly for higher angles of attack. This deterioration was believed to be related in part to model dynamics encountered during the test as the amount of flow separation on the model increased. Since the balance was sized to capture small differences in drag, the balance was unable to handle moderate amounts of dynamics without exceeding the axial beam limit. In the regions where the angle of attack was greater than 5 degrees or less than 1 degree, the model experienced noticeable oscillations, with the amplitude increasing to trigger balance limits as the angle was increased to about 7.5 degrees. However, in the region of 1 to 5 degrees, the uncertainty of the drag data was only about 0.3 counts.

E. Data Comparisons

The remaining figures in this paper provide a series of comparisons of the CFD predictions with results from the wind tunnel tests. Figures 33 and 34 compare the lift curves of the baseline and redesigned BLI configurations with elevons at zero and five degrees, respectively. The lift curve for the design is shifted slightly downward from the baseline for both elevon settings. The CFD accurately predicted this shift as well as the actual C_L values.

Results for pitching moment, the most difficult component for CFD to predict accurately, are shown in Fig. 35. The curves for the two configurations have very similar slopes at any given C_L, but the design curve has been shifted in the positive C_m direction relative to the baseline. This brings the design closer to trim at the cruise condition (C_L = 0.24), reducing the amount of elevon deflection needed to trim the aircraft and thus the trim drag. Although the CFD was able to match the experimental C_m at cruise conditions reasonably well, the pitch stability and the C_m increment between the baseline and design were under-predicted. Figure 36 shows similar results for the elevons at 5-degrees condition.

The lift vs. drag curve (Fig. 37) shows that up to the highest C_L computed for the baseline configuration, the redesign nacelles have reduced the drag. Over this region, CFD was able to predict the drag levels and increments reasonably well. Figure 38 shows a more detailed plot of the L/D characteristics around the cruise C_L. While the CFD slightly under-predicted the experimental L/D levels, the increment from baseline to redesign was matched fairly well. Figure 39 shows the values of the drag reduction obtained by the redesign nacelles for a given C_L. The two lines surrounding the x-axis represent the uncertainty of the data. The results indicate that the wind tunnel data closely matched the predicted drag improvement of 1.3 percent for the redesign configuration.

The effects of deflecting the two inboard elevons are shown in Figs. 40 and 41. Figure 40 shows the change in L/D caused by a 5-degree deflection. Overall, the deflection of the elevons produced a larger change in L/D on the design configuration than on the baseline, although at the cruise condition there is very little difference in the experimental data. The CFD predicted the increments between configurations and levels fairly well around the cruise condition, but the correlation deteriorates for lower and higher values of C_L.

Figure 41 shows elevon effectiveness for the 5-degree deflection in terms of pitching-moment increment. The CFD and experimental data indicate a fairly constant level of effectiveness for both the baseline and redesign across the C_L range. The small increase in elevon effectiveness at the cruise condition indicated for the redesign in the wind tunnel data was not picked up in the CFD results. It was a little surprising that the redesign did not show a greater increase in effectiveness, considering the reduction in flow separation for the design (see Fig. 17), but perhaps this indicates that the progression of separation on the two configurations is comparable for this amount of elevon deflection. The agreement between CFD and experiment shown in Fig. 40 and 41 seems to confirm that the simple modeling of the elevons in the CFD was adequate for examining overall forces and moments near cruise.

The elevon effectiveness data was combined with the overall shift of the C_m curve to estimate a trim drag benefit for the redesign configuration of about 0.8 percent. This brings the total drag reduction at cruise to about 2 percent. While this is not a huge benefit, it is significant considering the limited area involved in the redesign and the very reasonable flow conditions (e.g., weak nacelle shocks) for the baseline. The increment is very similar to that achieved using numerical optimization[10], although the baseline configuration in that study had what appeared to be fairly strong shocks and significantly more flow channeling effects than in the current investigation.

The chordwise pressure distributions at two span locations are shown in Figs. 42 and 43. These cuts were taken at cruise conditions: Mach 0.85, Reynolds number of 75 million, and an angle of attack of 4.2 degrees. The first cut, taken at η=0.10, goes through the middle of the elevon in between the two nacelles. The pressure distribution for the design matches the baseline distribution up to x/c=0.8, the location where the design changes begin. This indicates that, at least for this station, the design changes maintained the original level of circulation and thus tends confirm the validity of the zonal design approach in this area. The CFD was able to predict the decrease in the adverse pressure gradient due to the redesign near the trailing edge seen in the experimental results. The second cut, taken at η=0.21, extends to the inlet of the outboard nacelle. The CFD was able to predict the limiting of the pressure coefficient in the region in front of the redesign nacelle and, while levels are not identical, the increments are predicted fairly well.

F. Flow Visualization

As noted earlier, the primary approach to improving both aircraft performance and elevon effectiveness during the CFD design was to reduce the amount of boundary layer separation on the wing ahead of and between the nacelles. While the predicted drag reduction and pressure changes were generally confirmed by the wind tunnel data, these data provided little insight into whether or not the CFD separation results as shown in the SEP function contours were accurate. In a conventional wind tunnel, the boundary layer condition as indicated by surface flow direction is often visualized using various oil-flow techniques. This approach cannot be used in the NTF because of

the cryogenic temperatures required to get the highest Reynolds numbers. Fluorescent mini-tufts have been used in NTF with some success, but they are somewhat brittle and tend to be intrusive, especially with the thin boundary layers present at high Reynolds numbers. In the previous NTF test of the BWB under the AST Program, temperature sensitive paint (TSP) was used to indicate boundary layer transition from laminar to turbulent, but did not address turbulent boundary layer characteristics in the region of the trailing edge.

In an attempt to address the visualization of flow separation on the BWB, two experimental techniques were explored, with details of the development and results given in Watkins et al.[25]. The first utilized pressure sensitive paint (PSP) to show surface flow direction. Since the testing medium in NTF is nitrogen, there is no oxygen present to interact with the typical formulations of PSP. It was suggested by Dr. Keisuke Asai at Tohoku University in Japan, however, that air could be bled out through the pressure orifices and that this might create streak lines as the PSP reacted to the oxygen. Results from this technique along with a corresponding CFD prediction for the new BLI design with the elevons deflected 5 degrees are shown in Fig. 44. The results were obtained at the cruise Mach number and angle of attack, but at a Reynolds number of 20 million instead of 75 million. As discussed in Ref. 25, the colder temperatures required for the higher Reynolds number created some problems that degraded quality of the flow visualization. The predicted flow patterns match the PSP results fairly well, accurately representing the span-wise flow resulting from the boundary layer separation in front of and beside the nacelles as well as near the trailing edge of the elevon. In addition to the flow direction information, the PSP picture also reveals the location of the wing shock, running span-wise across the figure about 1 nacelle length ahead of the outboard nacelles. The shock location is slightly further aft in the CFD results, which is consistent with the higher Reynolds number used in the computations. It was thought that this feature is visible because the lights required for the PSP projected a shadow on the surface as in Schlierin photography as opposed to the PSP paint itself responding to a pressure difference.

The second flow visualization technique briefly investigated was the use of TSP to qualitatively identify regions where flow separation was present or imminent. Contour plots of CFD results indicated that wing temperature correlated well with the skin-friction based SEP function, and it was determined that one of the TSP formulations had a temperature range and sensitivity to match the test conditions. Unfortunately, the initial attempt was unsuccessful (probably due to too gradual of a temperature step imposed on the free-stream) and the testing schedule did not permit additional attempts.

IV. Concluding Remarks

The primary goal of this task within the UEET Project was to evaluate CFD design methods for use in propulsion/airframe integration and confirm their effectiveness through high-Reynolds number wind tunnel tests. During the course of this study, a number of conclusions and recommendations were developed relative to the CFD as well as the wind tunnel testing aspects of the program. First, the USM3D flow solver was shown to be sufficiently accurate for use in design, with good correlation demonstrated between its predictions and wind tunnel data from a previous BWB test in the NTF as well as the results of the current PAI tests. Particularly encouraging was the verification of fairly small changes in drag and local pressures between the baseline and design configurations. Elevon deflection effects were also predicted fairly well even though a crude grid model was used in the CFD. The unstructured grid approach used by USM3D simplified the implementation of the CDISC design methodology for this fairly complex geometry, eliminating the need to generate lengthy scripts to ensure the consistent projection of design changes onto the overlapping grids used in OVERDISC. In addition, the zonal design capability significantly reduced the time required to develop a successful design strategy, in one case providing a factor of 20 savings in time and memory relative to using the full grid. Finally, even though the USM3D/CDISC design system proved to be accurate and efficient in this PAI design effort, it is believed that an adjoint-base optimization method such as FUN3D, while perhaps not as efficient as CDISC, may provide larger performance improvements. There are currently plans in the UEET Project to evaluate both approaches in supersonic business jet PAI design applications.

In regard to the high-Reynolds number testing in NTF, the results generally confirmed the predicted design benefits. Balance and pressure instrumentation accuracies were well within the levels required to capture the small design changes and repeatability between runs was good. Because a sensitive balance was required to achieve this level of accuracy, however, there were some run conditions that could not be obtained due to model dynamic loads. While this did not impact the primary objectives of this test, it may be a concern for future stability and control testing. Also, even though the pressure instrumentation was fairly extensive in the region of the nacelles, it was felt more detail was needed to fully assess a PAI design. The initial results obtained with the bleed-air PSP technique were very encouraging in spite of some difficulties at the coldest temperatures. Further development of this technique, including accurate evaluation of its intrusiveness, is strongly recommend since it has application for any tests that involve separated flows. In addition, the TSP approach that was tried as well as a nitrogen-compatible PSP

capability could provide important detail without the need for large numbers of pressure orifices, and should be pursued.

References

[*] Liebeck, R, "Design of the Blended-Wing-Body Subsonic Transport," AIAA-2002-0002, January 2002.

[2] Daggett, David L., Kawai, Ron, and Friedman, Doug, "Blended Wing Body Systems Studies: Boundary Layer Ingestion Inlets With Active Flow Control," NASA CR-2003-212670, December 2003.

[3] Roman, D., Allen, J. B., and Liebeck, R. H., "Aerodynamic Design Challenges of the Blended-Wing-Body Subsonic Transport," AIAA-2000-4335, August 2000.

[4] Holmes, Stanley, "The Battle over a Radical New Plane," *Business Week*, Vol. 145, November 25, 2002, pp. 106-108.

[5] Clark, Lorenzo R., and Gerhold, Carl H., "Inlet Noise Reduction by Shielding for the Blended-Wing-Body Airplane," AIAA-99-1937, May 1999.

[6] Roman, Dino, Gilmore, Richard, Wakayama, Sean, "Aerodynamics of High-Subsonic Blended-Wing-Body Configurations," AIAA-2003-554, January 2003.

[7] NASA Aerospace Vehicle Systems Technology Office, EASI Updates, "The Slotted Wing", August 31, 2004, http://avst.larc.nasa.gov/projects_easi_updates.html.

[8] Kawai, Ronald T., Friedman, Douglas M., and Serrano, Leonel, "Blended Wing Body Boundary Layer Ingestion Inlet Configuration and Systems Studies," NASA CR (to be published).

[9] Rodriguez, David L.,"A 3D Multidisciplinary Design Method for Designing Boundary Layer Ingesting Inlets," AIAA-2000-0424, January 2000.

[10] Rodriguez, David L.,"A Multidisciplinary Optimization Method for Designing Boundary Layer Ingesting Inlets," AIAA-2002-5665, September 2002.

[11] Gorton, Susan Althoff, Owens, Lewis R,, Jenkins, Luther N., Allen, Brian G., and Schuster, Ernest P., "Active Flow Control on a Boundary-Layer-Ingesting Inlet," AIAA-2004-1203, January 2004.

[12] Campbell, Richard L., "Efficient Viscous Design of Realistic Aircraft Configurations," AIAA-98-2539, June 1998.

[13] Jespersen, D.C., Pulliam, T.H., and Buning, P.G., "Recent Enhancements to OVERFLOW," AIAA-97-0644, January 1997.

[14] Frink, N.T., "Assessment of an Unstructured-Grid Method for Predicting 3-D Turbulent Viscous Flows," AIAA-96-0292, January 1996.

[15]Frink, N.T., Pirzadeh, S.Z., Parikh, P.C., Pandya, M.J., and Bhat, M.K., "The NASA Tetrahedral Unstructured Software System," *The Aeronautical Journal*, Vol. 104, No. 1040, October 2000, pp.491-499.

[16] Nielsen, Eric J., and Anderson, W. Kyle, "Recent Improvements in Aerodynamic Design Optimization On Unstructured Meshes," AIAA 2001-0596, January 2001.

[17] Roe, P., "Characteristic Based Schemes for the Euler Equations," *Annual Review of Fluid Mechanics*, Vol. 18, 1986, pp. 337-365.

[18] Spalart, P., and Allmaras, S.A., "One-equation turbulence model for aerodynamic flows," AIAA 92-0439, January 1992.

[19] Menter, F.R., "Improved Two-Equation k-omega Turbulence Models for Aerodynamic Flows," NASA TM-103975, October 1992.

[20] Pandya, Mohagna J., and Frink, Neal T., "Aggomeration Multigrid for an Unstructured-Grid Flow Solver," AIAA-2004-0759, January 2004.

[21] Pirzadeh, S., "Three-Dimensional Unstructured Viscous Grids by the Advancing-Layers Method," *AIAA Journal*, Vol. 34, No. 1, January 1996, pp.43-49.

[22] Carter, Melissa Beth, "A computational Investigation of the Design Techniques for Propulsion Airframe Integration on a Blended Wing Body," Masters Thesis, School of Engineering and Applied Science, George Washington University, Washington DC, May 2004.

[23] Green, Bradford E., and Whitesides, John L., "Method for Designing Leading-Edge Fillets to Eliminate Flow Separation," *Journal of Aircraft*, Vol. 40, No. 2, March-April, 2003, pp. 282-289.

[24] Wahls, R., "The National Transonic Facility: A Research Retrospective," AIAA-2001-0754, January 2001.

[25] Watkins , A.N., Goad, W.K., Obara, C.J., Sprinkle, D.R., Campbell, R.L., Carter, M.B., Pendergraft, O.C., Jr., Bell, J.H., Schairer, E.T., Ingram, J.L., Oglesby, D.M., Underwood, P.J., and Humber, L.R., "Flow Visualization at Cryogenic Conditions Using a modified Pressure Sensitive Paint Approach," AIAA-2005-0456, January, 2005.

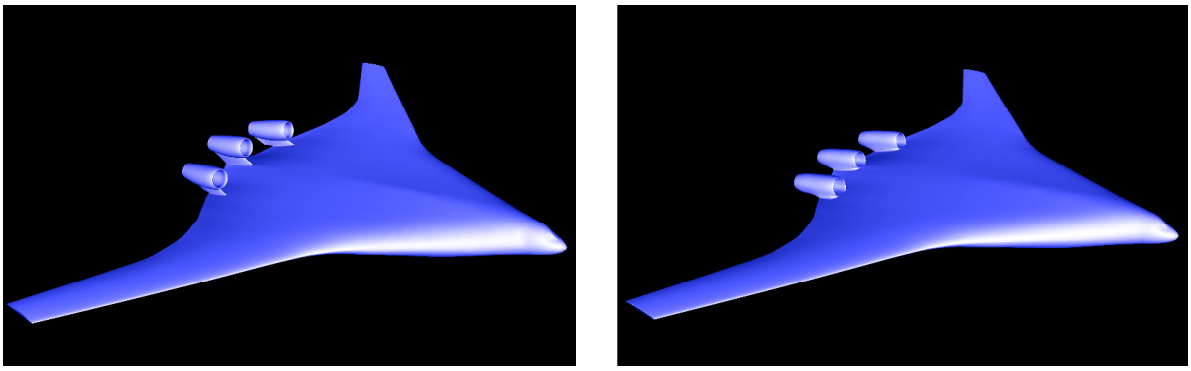

a) Strut mounted. b) Surface mounted (BLI).

Figure 1 BWB nacelle mounting approaches.

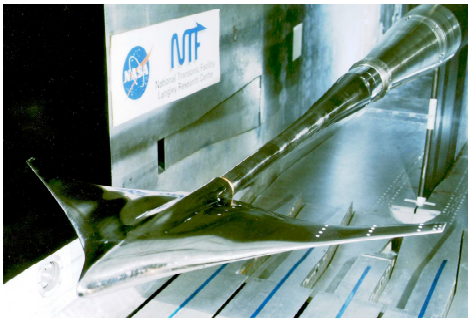

Figure 2 AST wing-only BWB model in NTF.

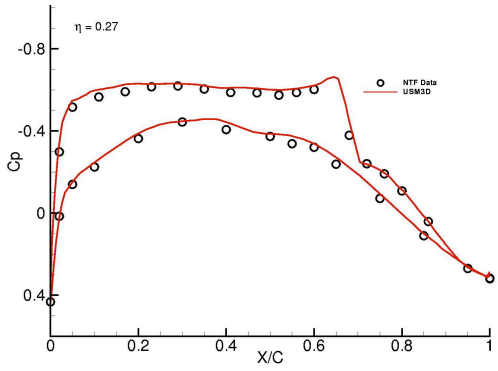

Figure 3 Correlation of CFD wing pressures with NTF data at cruise conditions.

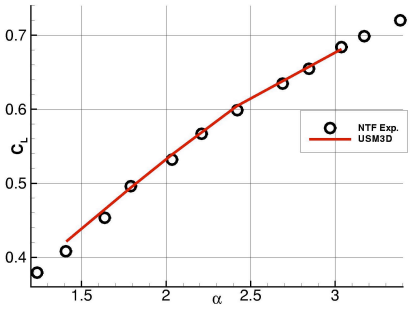

a) C_L vs. Alpha

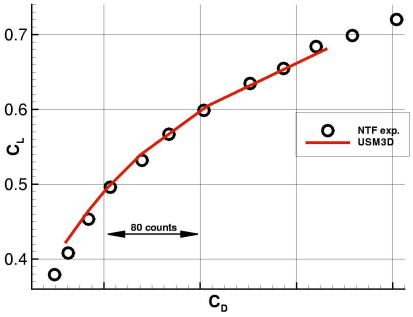

b) C_L vs. C_D

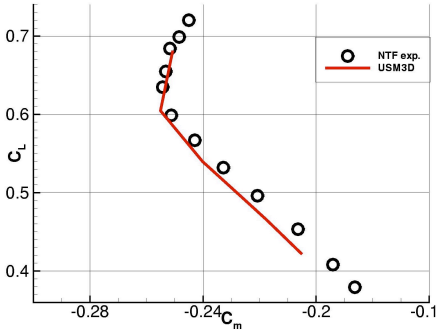

c) C_L vs. C_m

Figure 4 Correlation of CFD force and moment predictions with NTF data at cruise conditions.

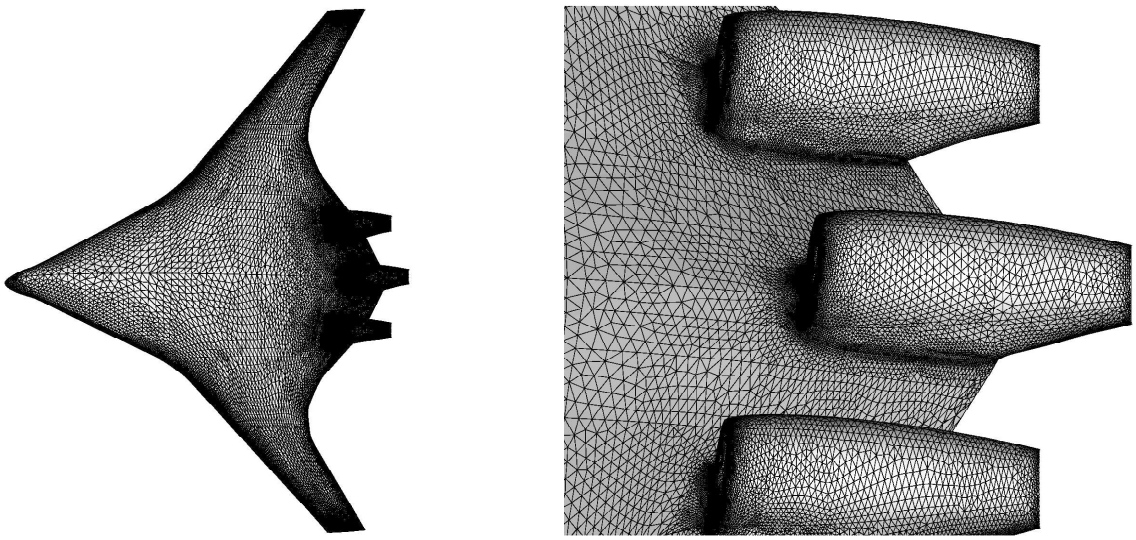

Figure 5 Unstructured grid for BWB with BLI nacelles.

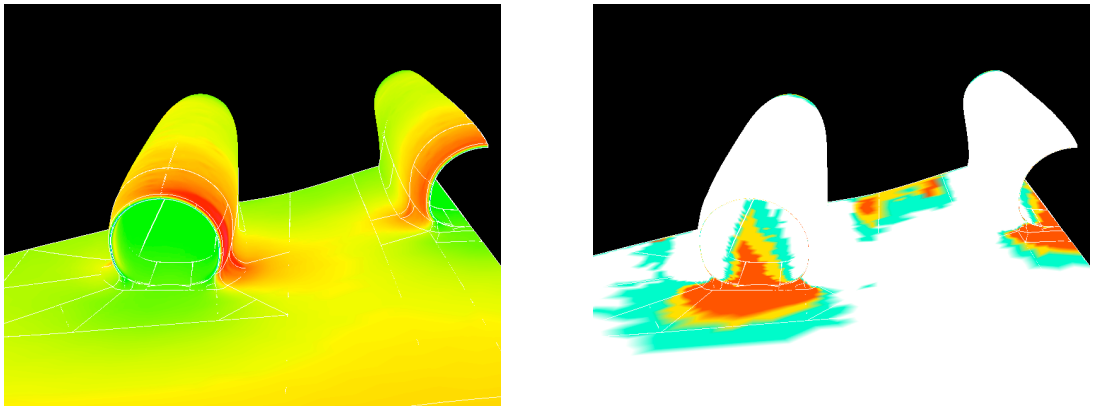

a) Mach **b) SEP function**

Figure 6 Flow contours from initial USM3D analysis at cruise conditions.

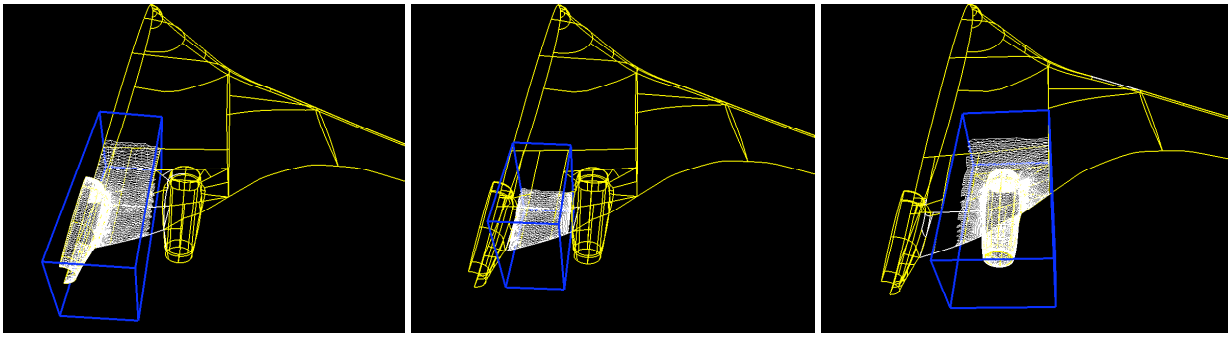

a) Inboard nacelle **b) Elevon** **c) Outboard nacelle**

Figure 7 Zonal grids used in CDISC design.

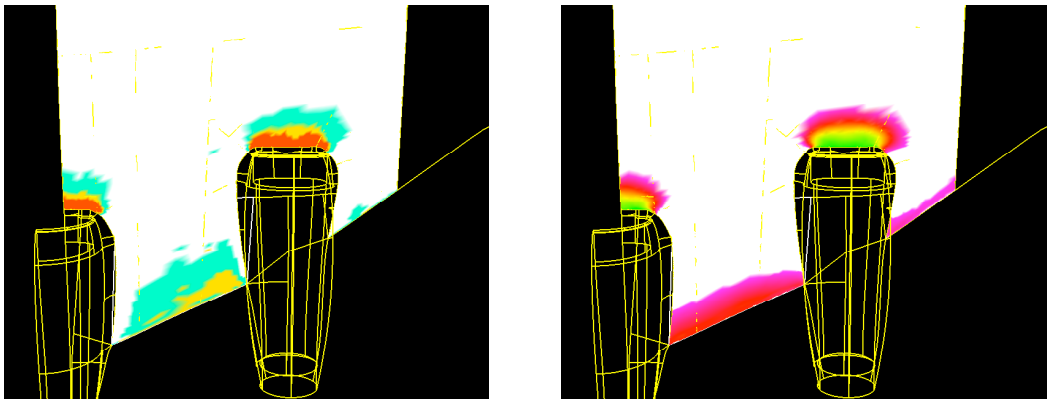

a) SEP function **b) $C_P > 0.2$ contours**

Figure 8 Correlation of boundary layer SEP function with pressure coefficient contours.

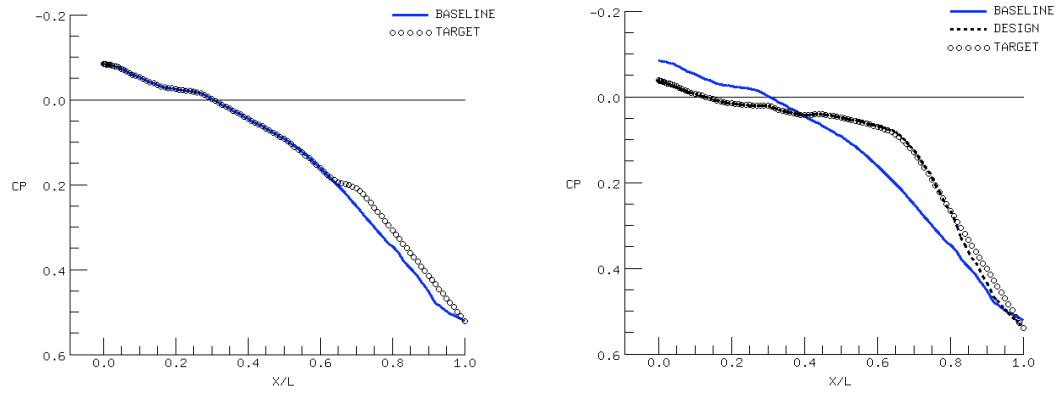

a) Initial **b) Final**

Figure 9 Target Pressure distributions for inboard nacelle design station.

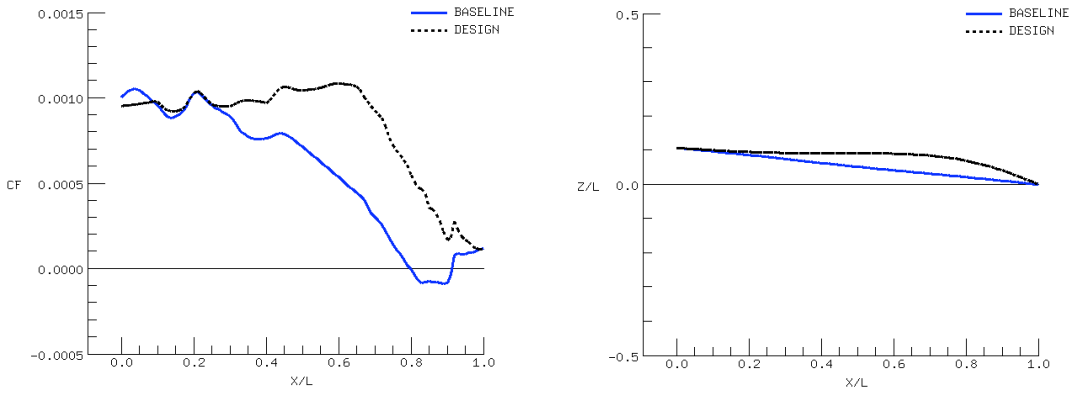

a) Skin-friction **b) Geometry**

Figure 10 CDISC design results for inboard nacelle design station.

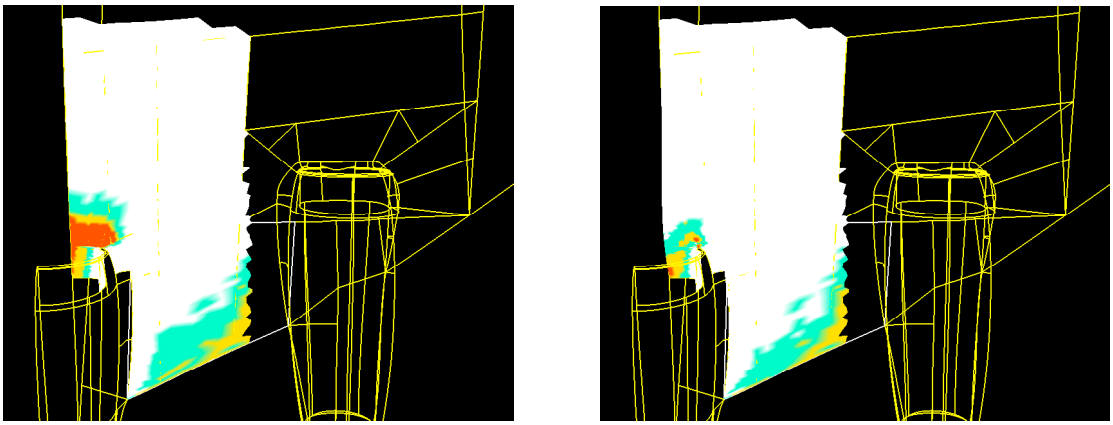

a) Baseline **b) Design**

Figure 11 SEP function contours for inboard nacelle zonal design.

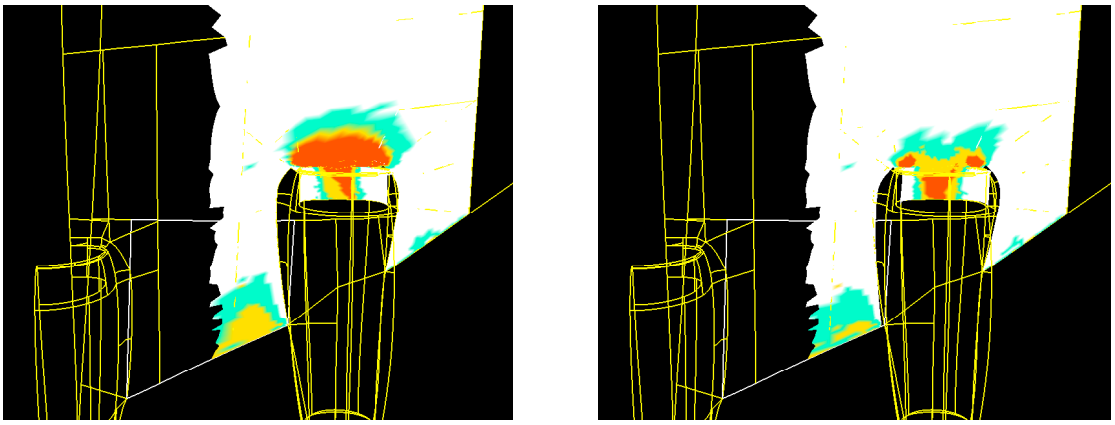

a) Baseline **b) Design**

Figure 12 SEP function contours for outboard nacelle zonal design.

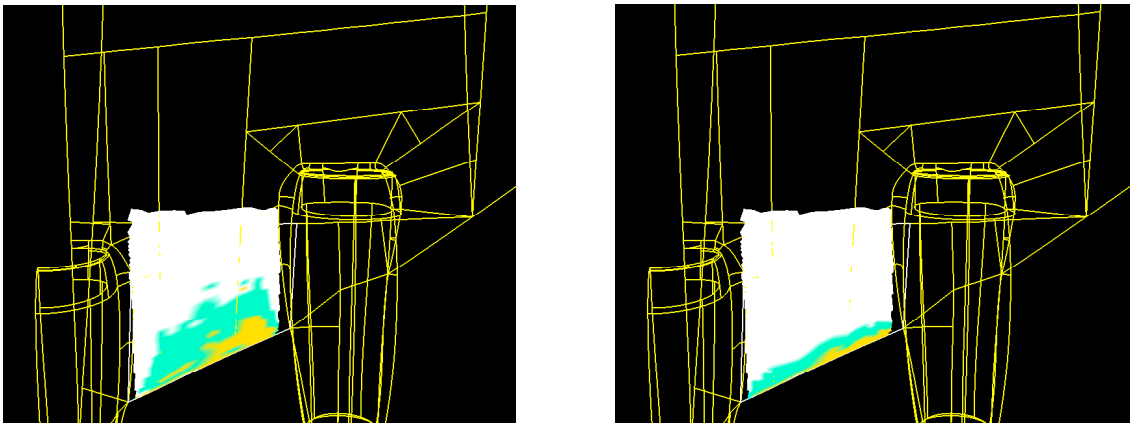

a) Baseline **b) Design**

Figure 13 SEP function contours for elevon zonal design.

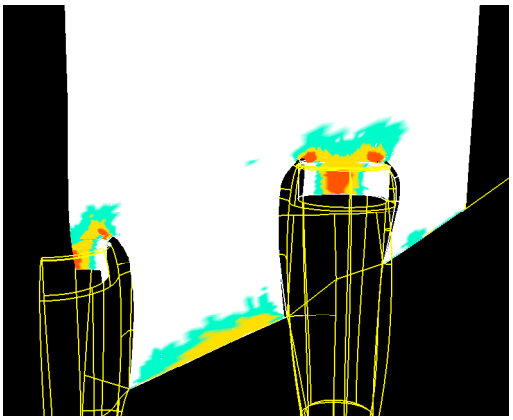

Figure 14 SEP function contours from full-grid analysis of final design.

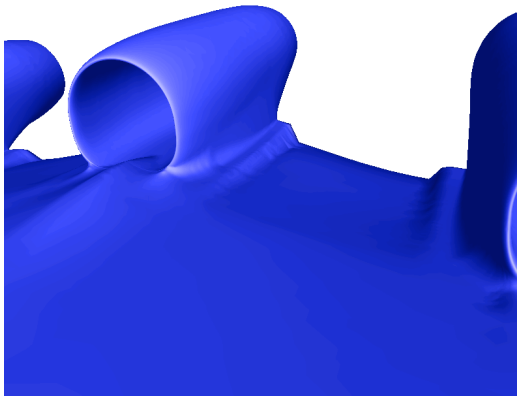

Figure 15 CFD modeling of elevon deflection.

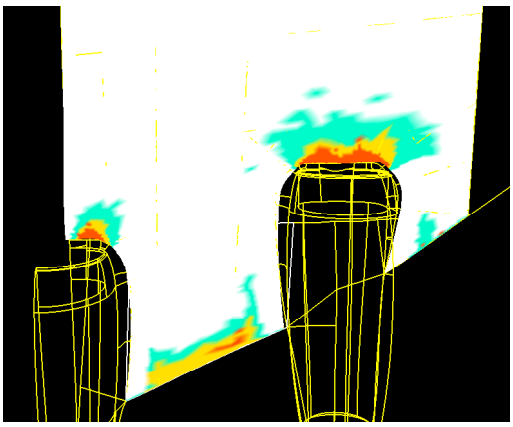

a) 0 degrees

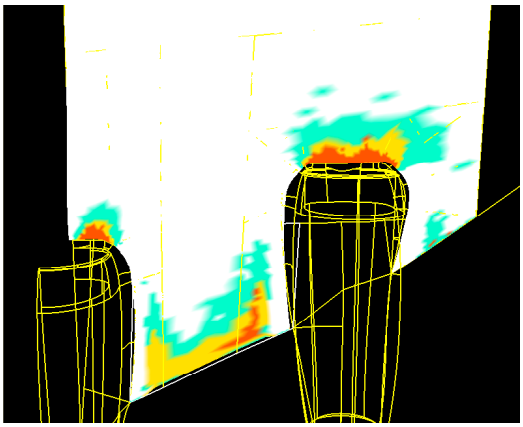

b) 5 degrees

Figure 16 Effect of final design elevon deflection on SEP function contours.

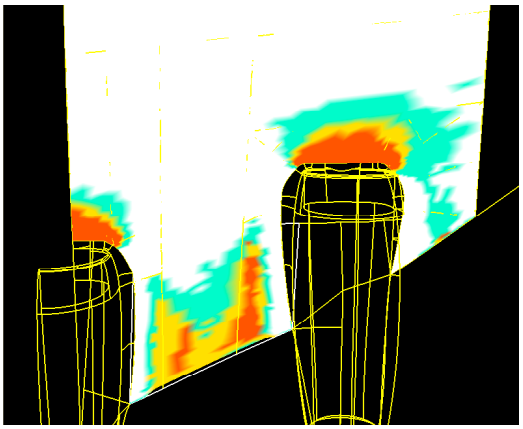

a) Baseline

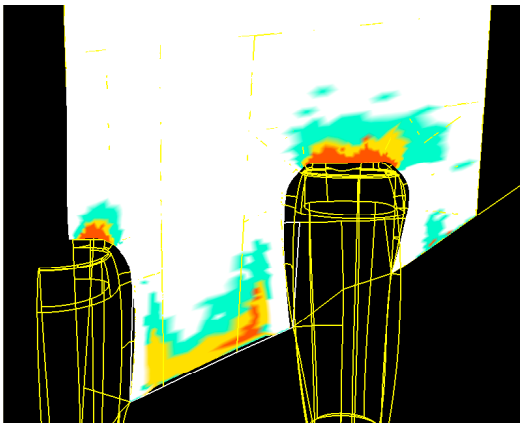

b) Design

Figure 17 Comparison of SEP function contours for the baseline and final design with 5 degrees of elevon deflection.

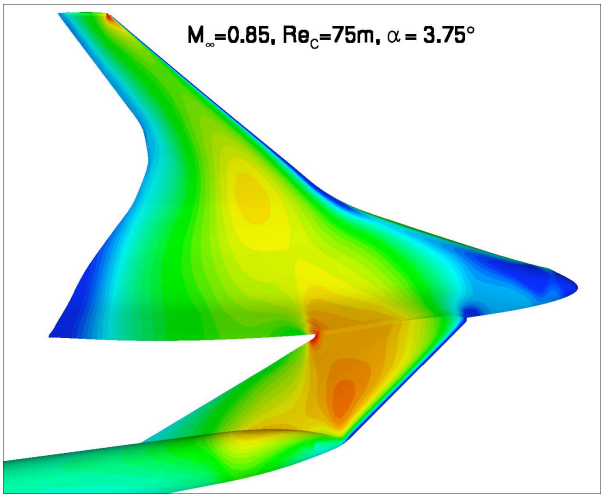

Figure 18 Pressure contours from OVERFLOW for wing-strut at cruise conditions.

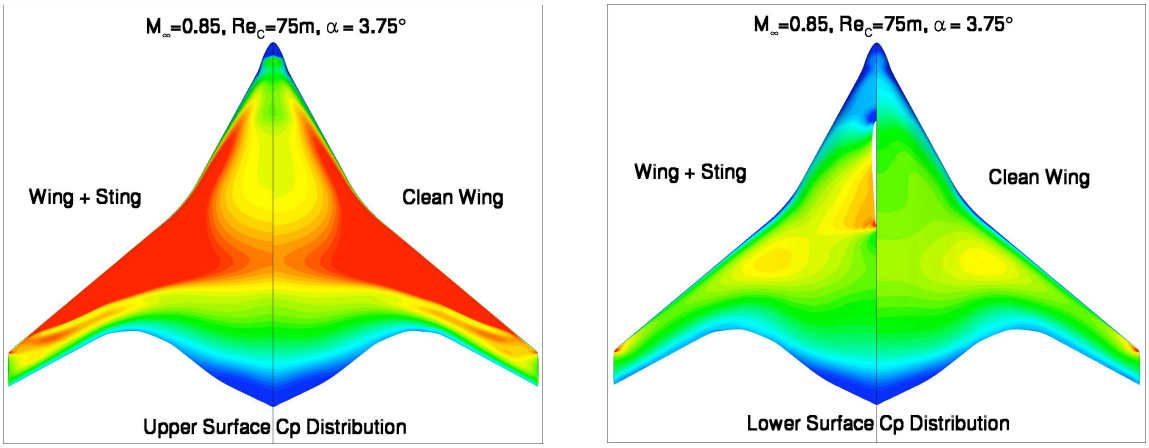

a) Upper surface **b) Lower surface**

Figure 19 Effect of strut on wing pressure coefficient contours at cruise conditions.

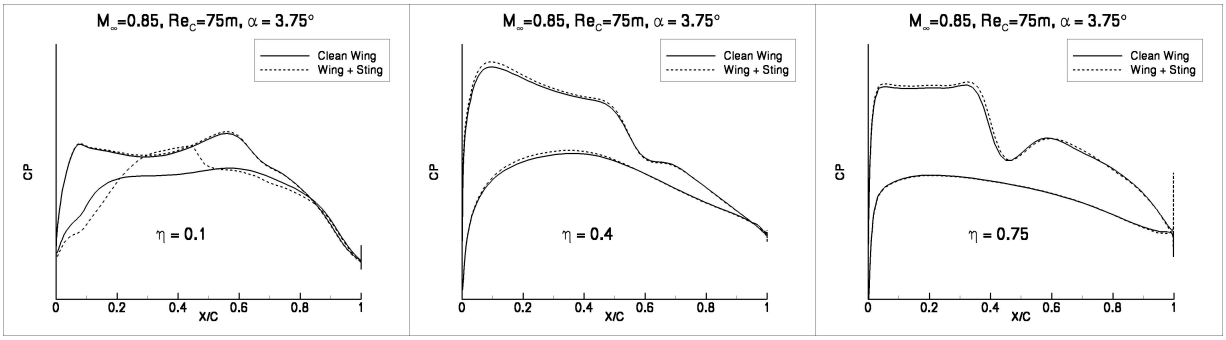

a) η=0.10 **b) η=0.40** **c) η=0.75**

Figure 20 Comparison of stream-wise pressure distributions for the wing-only and wing-strut configurations at cruise conditions.

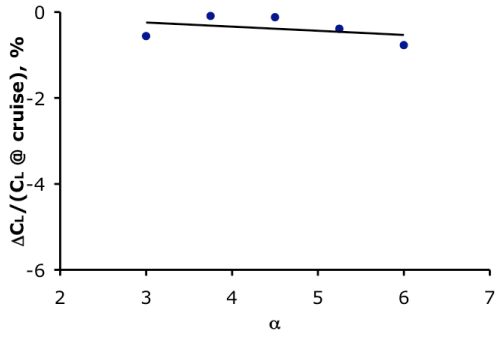

a) Lift

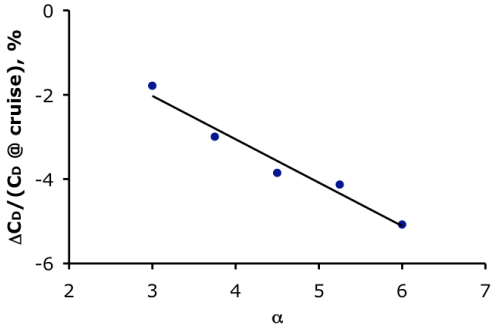

b) Drag

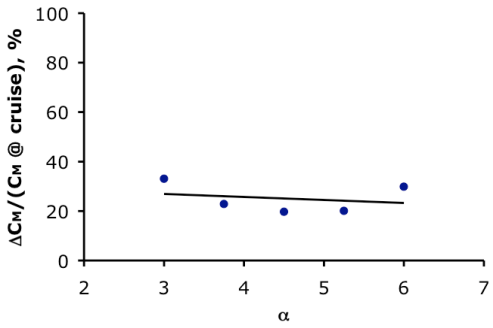

c) Pitching moment

Figure 21 Strut interference effects computed using OVERFLOW.

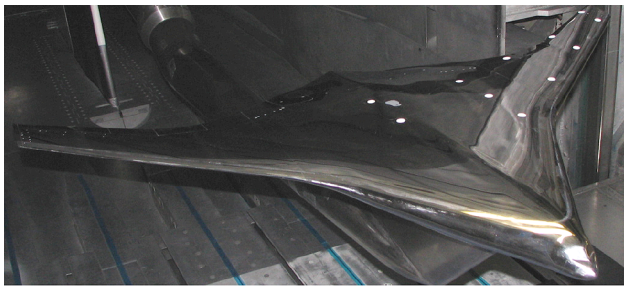

Figure 22 Clean wing configuration

Figure 23 Pylon mounted nacelles

Figure 24 Baseline BLI nacelles

Figure 25 Redesigned BLI nacelles

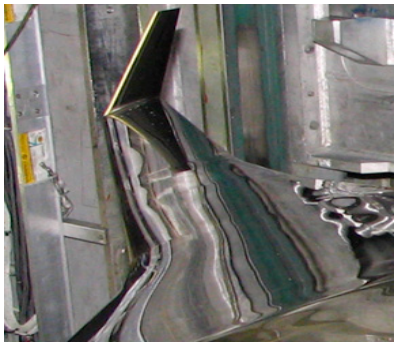

Figure 26 Model with winglets

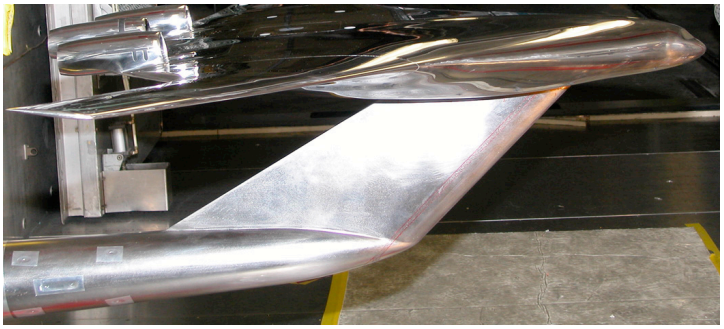

Figure 27 Lower swept-strut

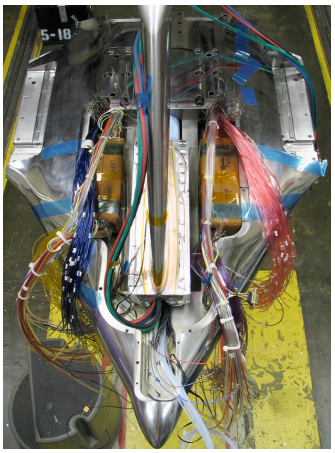

Figure 28 Model inverted in build-up bay showing limited room inside

Figure 29 Deflected elevons (5-degrees)

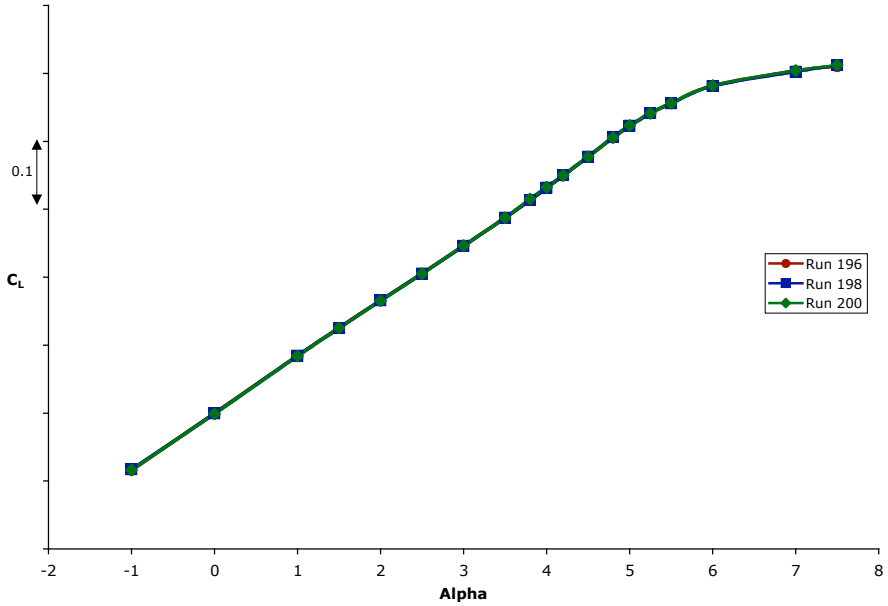

Figure 30 Repeatability of C_L for the baseline BLI configuration

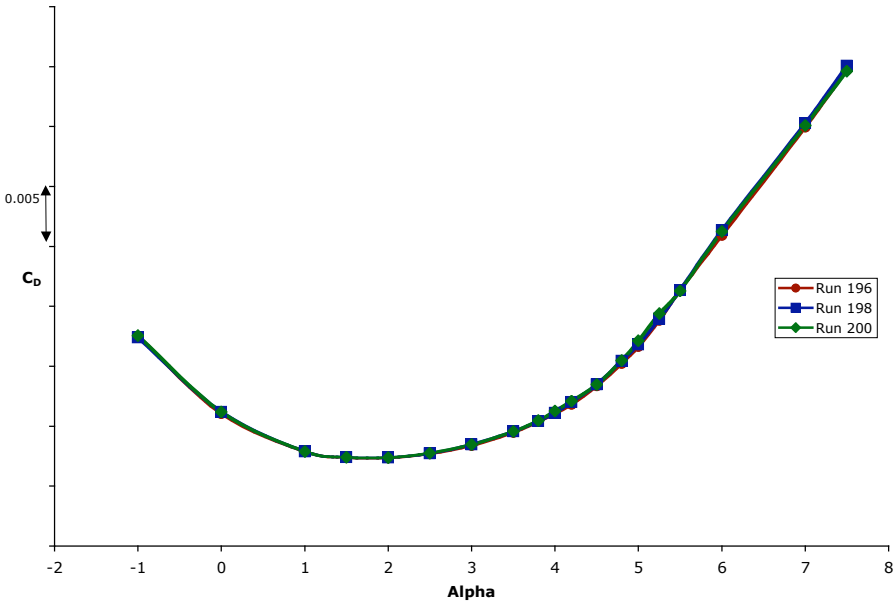

Figure 31 Repeatability of C_D for the baseline BLI configuration

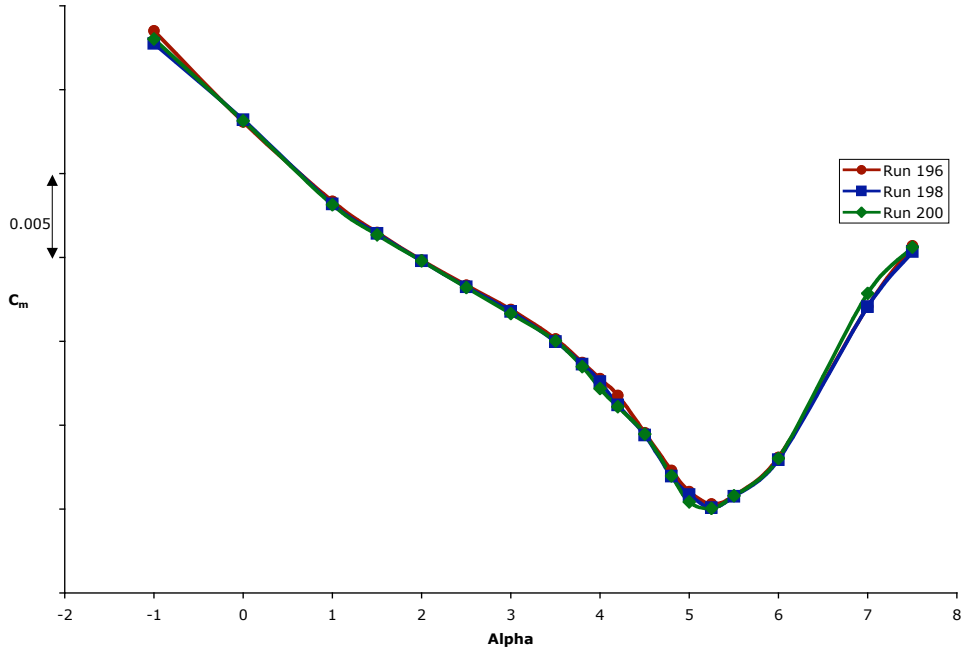

Figure 32 Repeatability of C_m for the baseline BLI configuration

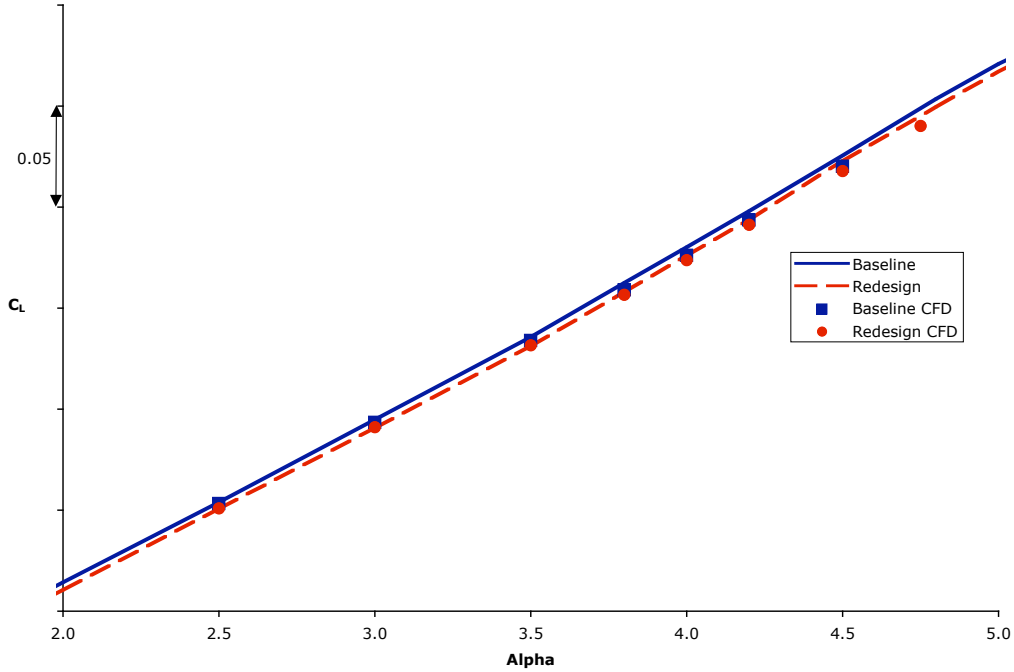

Figure 33 Wind Tunnel vs CFD lift curve comparisons

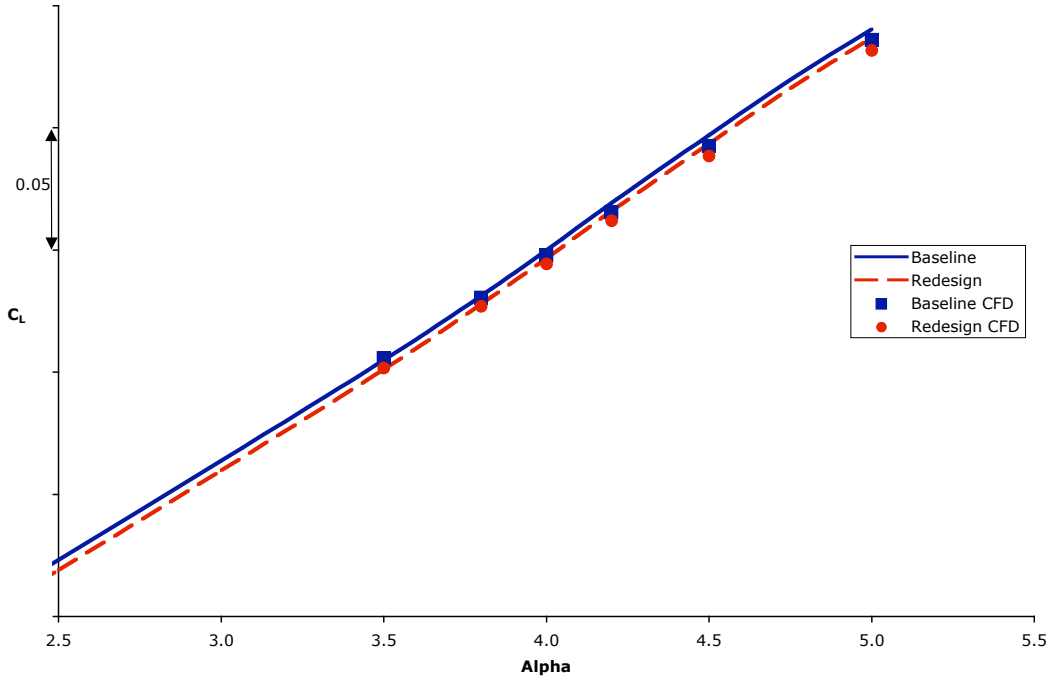

Figure 34 Lift curve comparisons with elevons at 5-degrees

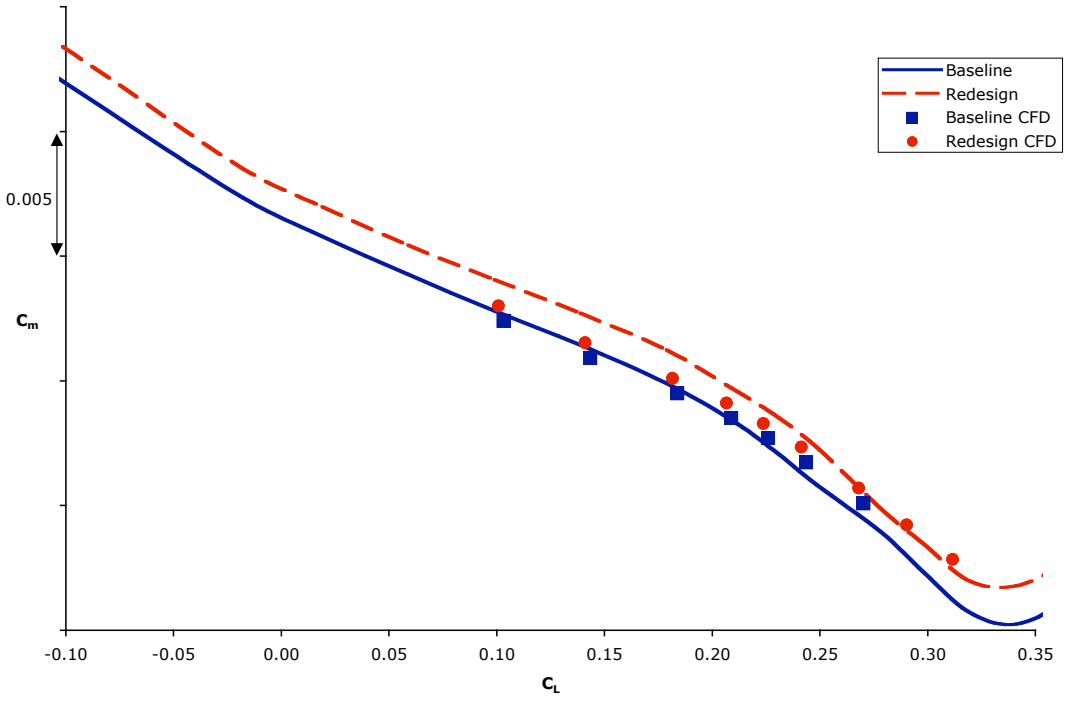

Figure 35 Pitching moment vs. lift comparisons

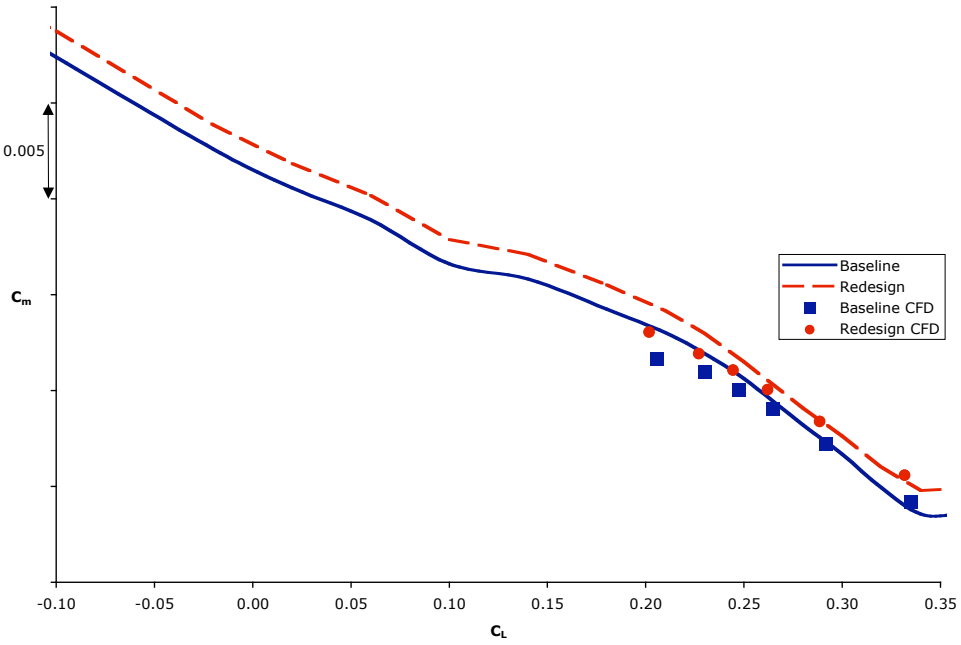

Figure 36 Pitching moment vs. lift comparisons with elevons at 5-degrees

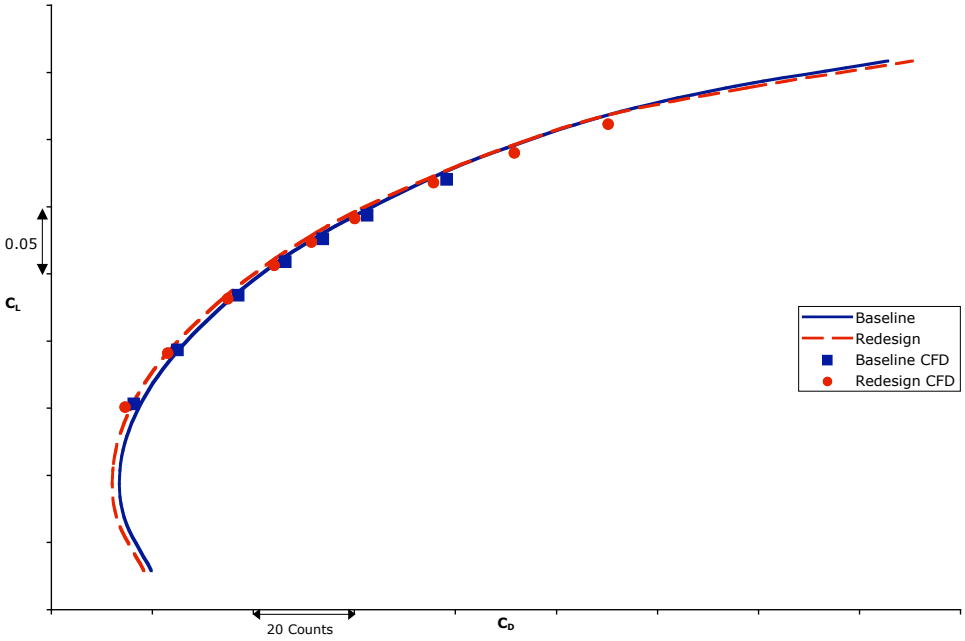

Figure 37 Lift vs. drag comparisons

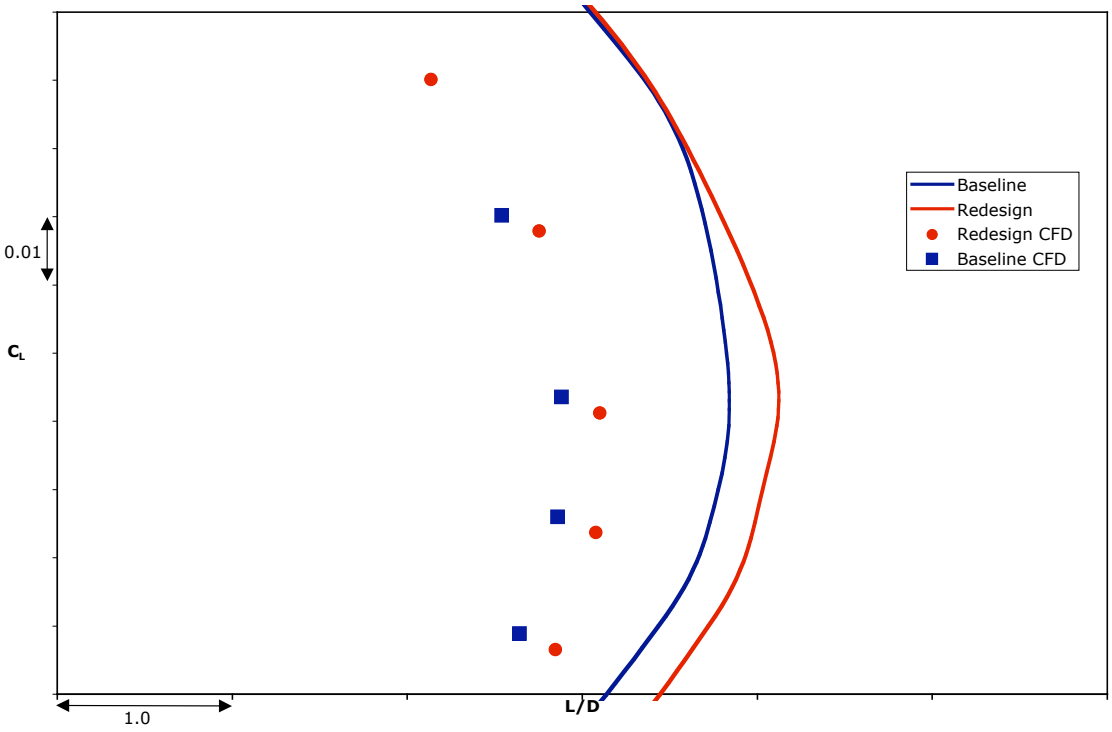

Figure 38 Lift vs. L/D comparisons

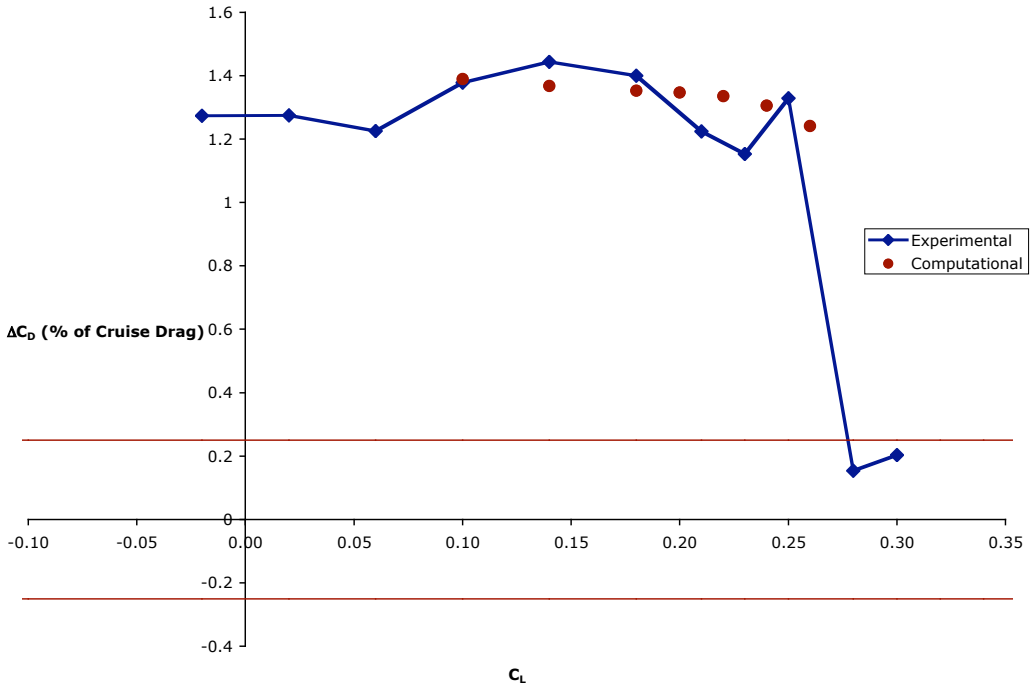

Figure 39 Wind tunnel vs. CFD drag reductions for redesign

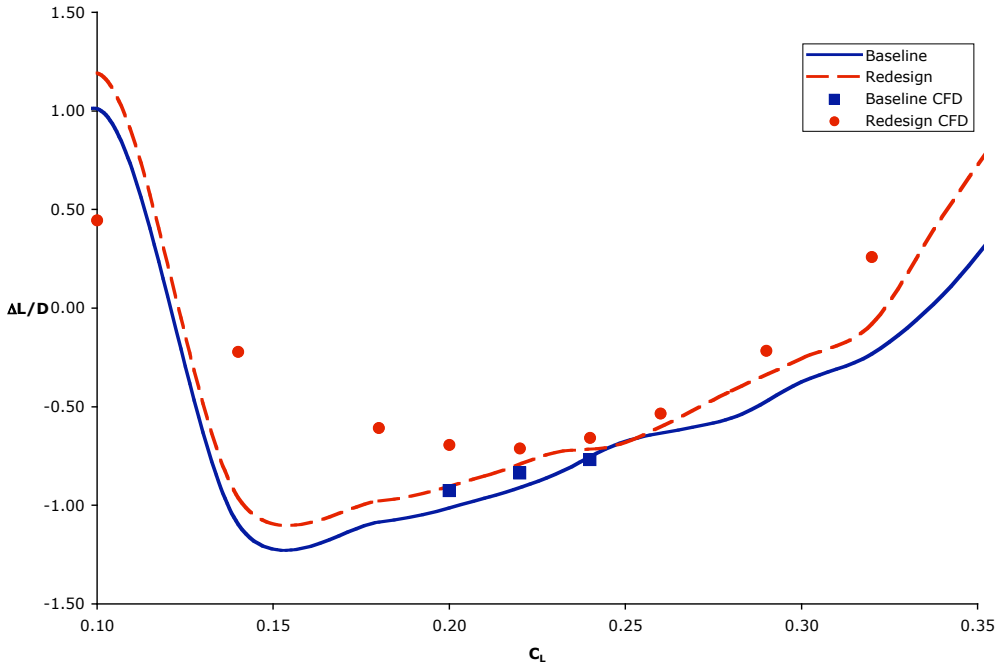

Figure 40 L/D increments for 5-degree elevon deflection

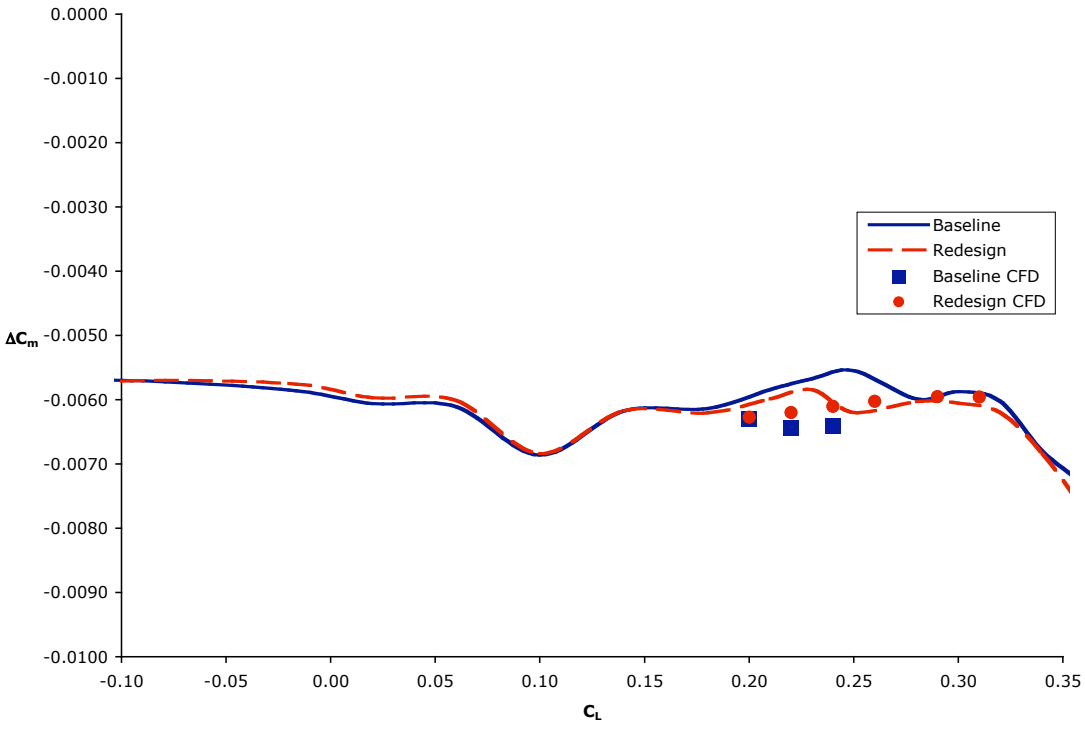

Figure 41 Pitching-moment increments for 5-degree elevon deflection

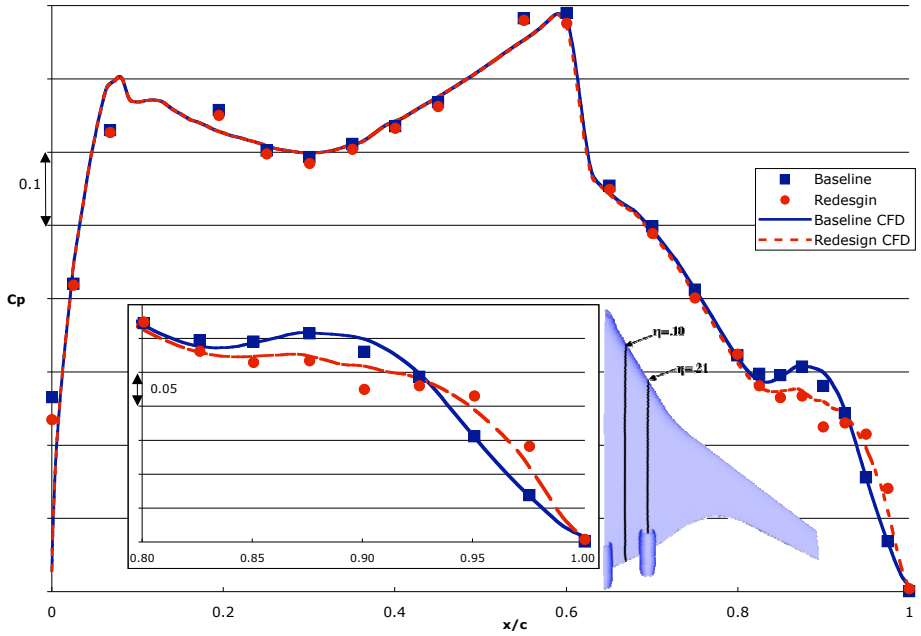

Figure 42 Comparison of C_P distribution at cruise conditions for η=.10.

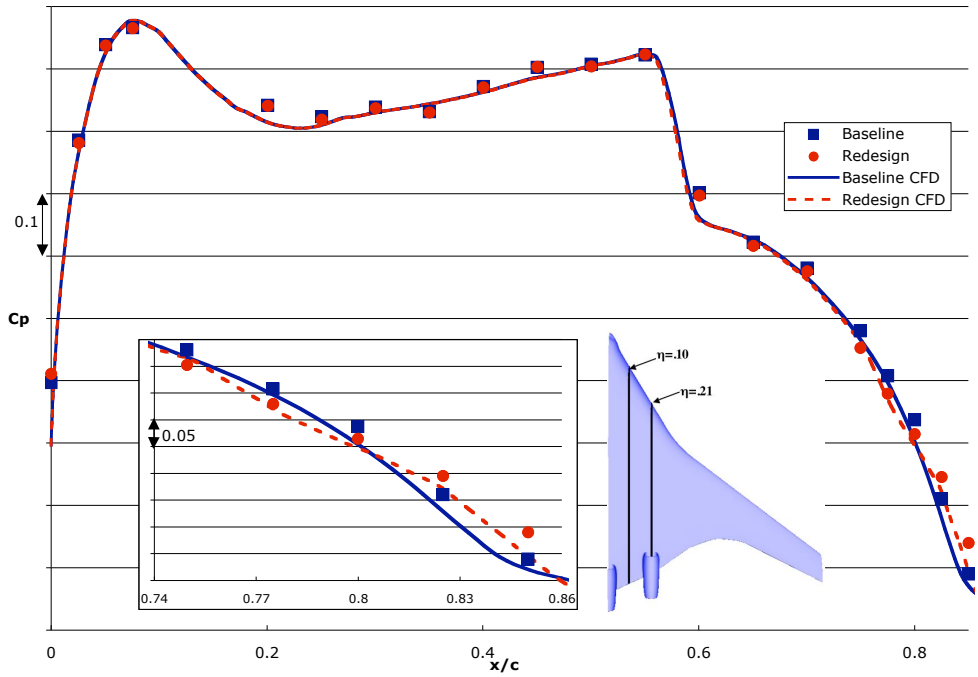

Figure 43 Comparison of C_P Distribution at cruise conditions for η=.21.

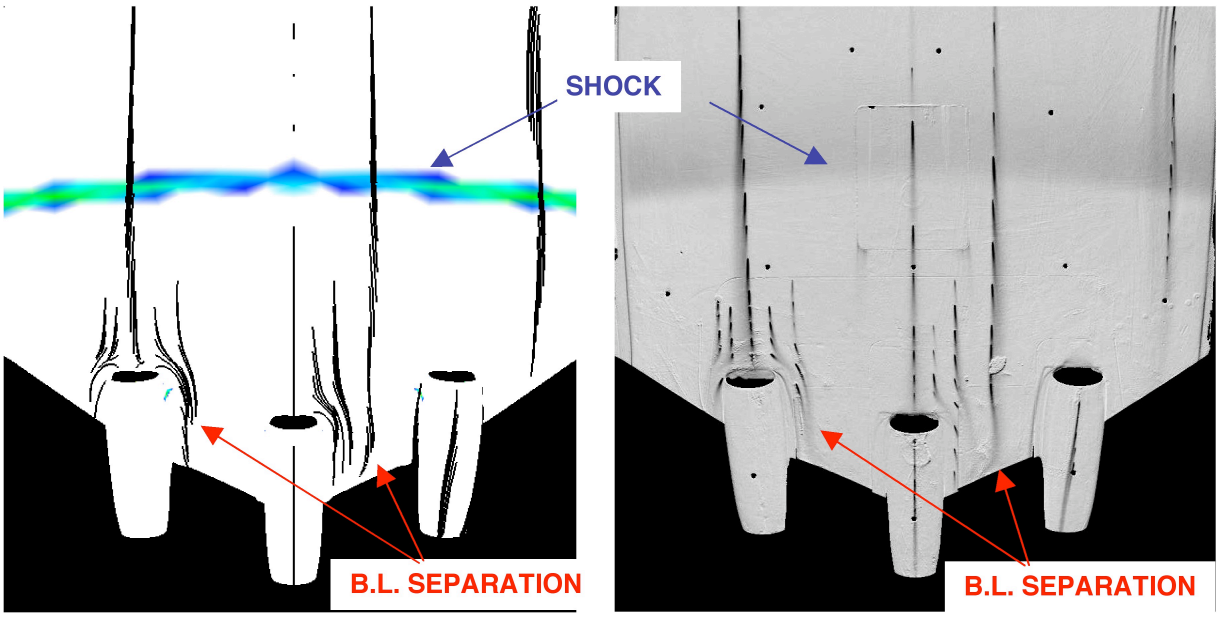

a) CFD **b) Wind tunnel**

Figure 44 Flow visualization results for the redesign with elevons deflected 5 degrees.